

Neuromechanics: From Neurons to Brain

Alain Goriely*, Silvia Budday†, Ellen Kuhl‡,1

*Mathematical Institute, University of Oxford, Oxford, United Kingdom

†Department of Mechanical Engineering, University of Erlangen–Nuremberg, Erlangen, Germany

‡Departments of Mechanical Engineering and Bioengineering, Stanford University, Stanford, United States

¹Corresponding author: e-mail address: ekuhl@stanford.edu

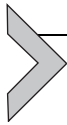
Contents

1. Motivation	80
2. Neuroelasticity	82
2.1 Elasticity of Single Neurons	82
2.2 Elasticity of Gray and White Matter Tissue	90
2.3 Elasticity of the Brain	93
3. Neurodevelopment	96
3.1 Growth of Single Neurons	96
3.2 Growth of Gray and White Matter Tissue	103
3.3 Growth of the Brain	106
4. Neurodamage	116
4.1 Neurodamage of Single Neurons	116
4.2 Neurodamage of Gray and White Matter Tissue	119
4.3 Neurodamage of the Brain	126
5. Open Questions and Challenges	128
Acknowledgments	131
Glossary	132
References	133

Abstract

Arguably, the brain is the most complex organ in the human body, and, at the same time, the least well understood. Today, more than ever before, the human brain has become a subject of narcissistic study and fascination. The fields of neuroscience, neurology, neurosurgery, and neuroradiology have seen tremendous progress over the past two decades; yet, the field of neuromechanics remains underappreciated and poorly understood. Here, we show that mechanical stretch, strain, stress, and force play a critical role in modulating the structure and function of the brain. We discuss the role of neuromechanics across the scales, from individual neurons via neuronal tissue to the whole brain. We review current research highlights and discuss challenges and potential future directions. Using the nonlinear field theories of mechanics, we illustrate three phenomena which are tightly regulated by mechanical factors: neuroelasticity, the

extremely soft behavior of the brain independent of time; neurodevelopment, the evolution of the brain at extremely long time scales; and neurodamage, the degradation of the brain at extremely short time scales. We hope that this review will become a starting point for a multidisciplinary approach to the mechanics of the brain with potential impact in preventing, diagnosing, and treating neurological disorders.



1. MOTIVATION

Embedded in the skull, surrounded by the cerebrospinal fluid, and enveloped by the meninges, our brain is remarkably well protected and mechanically isolated from its environment (Nolte, 2009). It is no surprise that many scientists believe that its mechanical behavior is entirely irrelevant to its structure and function. Over the past two decades, however, we have come to realize that virtually all of the 210 different cell types in our body respond to mechanical factors, and that mechanotransduction plays a critical role in regulating numerous intra- and extracellular events (Alberts et al., 2014). There seems no evident reason why the cells in our brain—mainly neurons and glial cells—should be insensitive to mechanical signaling (Franze, Janmey, & Guck, 2013).

The average human brain consists of about 100 billion neurons. The mechanical behavior of individual neurons has been extensively studied, however, almost exclusively in complete isolation (Bray, 1984; Heidemann, Lamoureux, & Buxbaum, 1997; Suter & Miller, 2011). Despite the common belief that neurons are the most significant cell type in our brain, glial cells—astrocytes, oligodendrocytes, and microglia—outnumber neurons by far (Alberts et al., 2014). Glial cells provide important protection and structural support for our neurons; yet, their mechanical function is not entirely clear. We are only beginning to understand how the different cell types in the brain interact, how this interaction influences the mechanical properties of neuronal tissue and, ultimately, how the brain functions as a whole (Goriely et al., 2015). Figure 1 illustrates the three relevant scales highlighted in this review, the cell, tissue, and organ levels.

During development, most tissues are initially extremely soft, but they increase in stiffness as they mature. Neuronal tissue is amongst the first to reach maturity and, as a result, remains the softest tissue in our body. With a stiffness on the order of kilopascals (Budday et al., 2014), it is seven orders of magnitude softer than most engineering materials, six orders of magnitude softer than bone, and four orders of magnitude softer than rubber (Bilston,

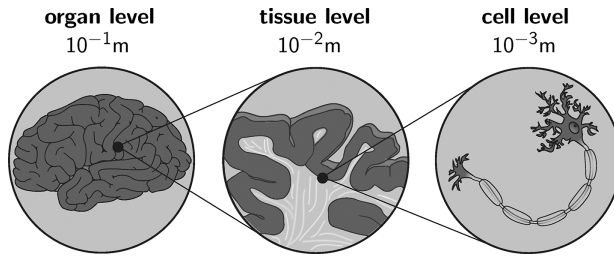


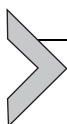
Figure 1 Multiscale model of the human brain. Organ scale with the whole brain (left), tissue scale with gray and white matter tissue (middle), and cellular scale with an individual neuron (right).

2011; Miller, 2011). Undoubtedly, testing, modeling, and understanding ultrasoft materials is tremendously challenging (Suo, 2012): In extremely soft matter, even very small physical perturbations away from the equilibrium state are capable of inducing large structural changes (Li, Cao, Feng, & Gao, 2012). In the brain, this paradigm plays a central role during development, gyrogenesis, and pattern selection (Budday, Steinmann, & Kuhl, 2015a; Sun & Hevner, 2014).

By virtue of its extreme softness, the human brain displays a wide variety of mechanical features: Under small deformations, our brain is essentially elastic and its deformations are almost entirely reversible (Chatelin, Constantinesco, & Willinger, 2010). Under large deformations, our brain becomes inelastic. The type of inelasticity is not unique though; it critically depends on the deformation rate and the time scale under consideration (Fallenstein, Hulce, & Melvin, 1969). Over long time scales, the brain is capable of adapting to environmental cues (Richman, Stewart, Hutchinson, & Caviness, 1975; Van Essen, 1997). A typical example is cortical folding during brain development, a process associated with time scales on the order of weeks or months (Raybaud & Widjaja, 2011). Over short time scales, the brain is incapable of adapting and becomes vulnerable to damage (McIntosh et al., 1998). A typical example is traumatic brain injury, a process associated with time scales on the order of milliseconds (Morrison III, Saatman, Meaney, & McIntosh, 1998).

For individual neurons, the three phenomena of elasticity, growth, and damage have been extensively studied and are now reasonably well understood. For nervous tissue, we are only beginning to understand the implications of elasticity, growth, and damage. For the living brain, we are far from understanding elasticity, growth, and damage, and have an even less complete picture of its neuromechanics as a whole. Traditionally, the notion

of neuromechanics has been associated with the control of human or animal movement by the nervous system. Here, we propose to challenge this view and refer to *neuromechanics* as the study of all mechanical effects, either controlled by the nervous system, or relevant to the function, structure, development, and response of the brain under physical forces. Conceptually, this can include biological, chemical, electrical, or thermal fields that bring about changes in the relevant physical fields. Typical examples are cell densities, chemical potentials, ion concentrations, electrical charges, and temperature changes that may enter the thermodynamic nonequilibrium and directly affect the physical forces, stress, stretch, strain, or stiffness of the brain. With this broader perspective in mind, the objective of this review is to stimulate discussion towards a more holistic, multiscale and multiphysics view of the brain through the lens of neuromechanics.



2. NEUROELASTICITY

Under small deformations, our brain is essentially elastic and its deformations are almost entirely reversible. In this section, we focus on the neuroelasticity of the brain. Specifically, we restrict our attention to phenomena that take place on relatively slow time scales, where viscous effects play a less significant role. We highlight the elasticity of single neurons in Section 2.1, the elasticity of gray and white matter tissue in Section 2.2, and the elasticity of the brain in Section 2.3. Whenever possible, we complement the theory with experiments reported in the literature, illustrate what we can learn from these experiments, and discuss how these findings at the individual scales contribute to our overall understanding of the brain as a whole.

2.1 Elasticity of Single Neurons

The one-dimensional elasticity of single neurons, or rather their axonal and dendritic processes, has been widely studied over the past three decades (Bray, 1984). Axons and dendrites connect the cell bodies of different neurons and transmit information between them (Roossien, Lamoureux, & Miller, 2014). Axons are made up of densely packed microtubules and neurofilaments, embedded in an actin cortex. Cross-linking tau proteins stabilize these microtubules and establish a homeostatic equilibrium state of axonal tension (Franze, 2013). Surrounded by a thick dielectric layer, the myelin sheath, axons make up the majority of the white matter tissue in our brain. To characterize the elasticity of single axons, or neurites in

general, we introduce the axonal stretch λ , the ratio of the unstretched axonal length L and the stretched axonal length l ,

$$\lambda = l / L . \quad (1)$$

In a three-dimensional continuum setting, the stretch generalizes to the deformation gradient F and introduces the left and right Cauchy Green deformation tensors, which, in one dimension, are simply the stretch squared, $C = \lambda^2$ and $b = \lambda^2$. A common constitutive model for soft biological materials is the Mooney Rivlin model (Mooney, 1940; Rivlin, 1948). Its free energy,

$$\psi = c_1 [I_1 - 3] + c_2 [I_2 - 3] , \quad (2)$$

is parametrized in terms of the first and second strain invariants, I_1 and I_2 , weighted by two phenomenological material parameters, c_1 and c_2 , which relate to the shear modulus μ as $\mu = 2 [c_1 + c_2]$. With only two parameters, the Mooney Rivlin model has become immensely popular, mainly because it is relatively easy to calibrate: It is highly successfully at modeling the elastic features of brain tissue (Bilston, Liu, & Phan-Thien, 2001; Hrapko, van Dommelen, Peters, & Wismans, 2006), and it outperforms other constitutive models in capturing the shear response of mammalian brain tissue, especially in the linear regime (Rashid, Destrade, & Gilchrist, 2013). In a three-dimensional setting, the three invariants take the following general representation in terms of the three principal stretches λ_1 , λ_2 , and λ_3 ,

$$I_1 = \lambda_1^2 + \lambda_2^2 + \lambda_3^2 \quad I_2 = \lambda_1^2 \lambda_2^2 + \lambda_2^2 \lambda_3^2 + \lambda_3^2 \lambda_1^2 \quad I_3 = \lambda_1^2 \lambda_2^2 \lambda_3^2 . \quad (3)$$

In the case of incompressibility, $J = \lambda_1 \lambda_2 \lambda_3 \doteq 1$, and uniaxial tension, $\lambda_1 = \lambda$ and $\lambda_2 = \lambda_3 = 1/\lambda^{1/2}$, the invariants are simply a function of the uniaxial stretch λ along the axon (1),

$$I_1 = \lambda^2 + \frac{2}{\lambda} \quad I_2 = 2\lambda + \frac{1}{\lambda^2} \quad I_3 = 1 . \quad (4)$$

Here, we have adopted the common assumption that there is no lateral constraint on the axon (Dennerll, Lamoureux, Buxbaum, & Heidemann, 1989), and the axon is free to contract laterally to maintain its volume when being stretched (Lamoureux, Heidemann, Martzke, & Miller, 2010). The Mooney Rivlin energy can then be parameterized exclusively in terms of the axonal stretch λ ,

$$\psi = c_1 \left[\lambda^2 + \frac{2}{\lambda} - 3 \right] + c_2 \left[2\lambda + \frac{1}{\lambda^2} - 3 \right]. \quad (5)$$

From the Clausius Duhem inequality, the Piola stress P , the stress across the axon, follows as thermodynamically conjugate to the axonal stretch λ ,

$$P = \frac{\partial \psi}{\partial \lambda} = 2 \left[c_1 + c_2 \frac{1}{\lambda} \right] \left[\lambda - \frac{1}{\lambda^2} \right]. \quad (6)$$

Its pull back introduces the Piola Kirchhoff stress $S = \lambda^{-1}P$,

$$S = 2 \frac{\partial \psi}{\partial C} = \frac{\partial \psi}{\partial \lambda} \frac{\partial \lambda}{\partial C} = \frac{1}{\lambda} P = 2 \left[c_1 + c_2 \frac{1}{\lambda} \right] \left[1 - \frac{1}{\lambda^3} \right], \quad (7)$$

its push forward introduces the Kirchhoff stress $\tau = P \lambda$,

$$\tau = 2 \frac{\partial \psi}{\partial b} b = 2 \frac{\partial \psi}{\partial \lambda} \frac{\partial \lambda}{\partial b} b = P \lambda = 2 \left[c_1 + c_2 \frac{1}{\lambda} \right] \left[\lambda^2 - \frac{1}{\lambda} \right]. \quad (8)$$

In case of incompressibility, $J = 1$, the one-dimensional Kirchhoff stress is identical to the Cauchy stress, $\sigma = \tau/J = \tau$. A popular technique to study the stress–stretch response of individual axons, is to pull an axon with a calibrated microneedle and analyze the equilibrium between the applied pulling force and the deformation of the axon (Bray, 1984). The equilibrium equation follows from the principle of virtual work by minimizing the total work W as the sum of the internal and external work W^{int} and W^{ext} ,

$$W = W^{\text{int}} + W^{\text{ext}} \rightarrow \min. \quad (9)$$

The internal work W^{int} is the work of the axon as it deforms upon stretch, $W^{\text{int}} = \int_{\mathcal{B}_0} \psi dV$. For simplicity, most experiments assume that the deformation φ and the cross section A are homogeneous along the axonal length L , $\int_{\mathcal{B}_0} \{\circ\} dV = \{\circ\} AL$. The external work W^{ext} is the work of the microneedle as it pulls on the axon with an external force F to induce the deformation φ ,

$$W^{\text{int}} = \psi AL \quad \text{and} \quad W^{\text{ext}} = -F\varphi. \quad (10)$$

The minimum of the total work, $W \rightarrow \min$, is equivalent to the vanishing first variation,

$$\delta W = \delta W^{\text{int}} + \delta W^{\text{ext}} \doteq 0 \quad \forall \delta \varphi. \quad (11)$$

With the variations of the internal and external work,

$$\delta W^{\text{int}} = AL P \frac{d\lambda}{d\varphi} \delta\varphi \quad \text{and} \quad \delta W^{\text{ext}} = -F \delta\varphi, \quad (12)$$

the principle of virtual work,

$$\delta W = \left[P AL \frac{d\lambda}{d\varphi} - F \right] \delta\varphi \doteq 0 \quad \forall \delta\varphi, \quad (13)$$

introduces the force–deformation relation of the microneedle experiment,

$$F = PAL \frac{d\lambda}{d\varphi}. \quad (14)$$

In a finite deformation setting, the derivative $d\lambda/d\varphi$, depends on the particular experimental setup and is different for axons pulled along their length and orthogonal to it. In the following, we illustrate these two conditions, since both experiments are equally common in the literature.

2.1.1 Example: Axial Tension Testing of Axons

Tension testing along the axon is also known as direct axial method (Dennerll et al., 1989). In the direct axial method, the distal end of the axon, the growth cone, is attached to a soft, calibrated glass needle, which is mounted a short distance away from a stiff reference needle. In a displacement–controlled, single axial movement, the stiff needle is pulled away from the axon using a micromanipulator. The deformation of the soft glass needle quantifies the force induced by pulling. By comparing this force against the axonal elongation, we can characterize the axonal stiffness. Figure 2 illustrates the microneedle experiment with axial axonal deformation.

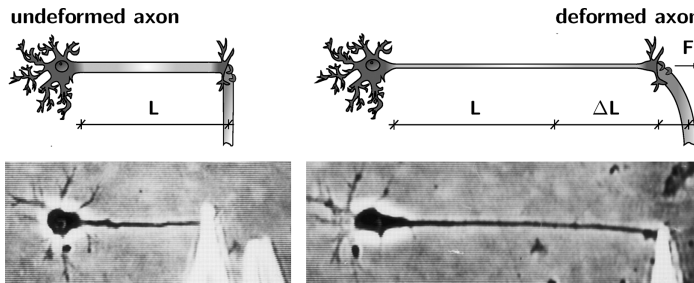


Figure 2 Microneedle experiment to probe the stiffness of single axons through controlled axial deformation (Ingber, Heidemann, Lamoureux, & Buxbaum, 2000). Undeformed axon of length L with the needle in contact at bright spot (left) and deformed axon of length $l = L + \Delta L$ after axial pulling with a needle force F (right).

The kinematics of the axial microneedle experiment are defined through the deformation φ , the initial axonal length L , the deformed axonal length l , the axonal stretch $\lambda = l/L$, and its derivative $d\lambda/d\varphi$,

$$l = L + \Delta L = \varphi \quad \lambda = \frac{\varphi}{L} \quad \frac{d\lambda}{d\varphi} = \frac{1}{L}.$$

For axially pulled axons, the general force-deformation relation (14) takes the following explicit form,

$$F = PA = SA \frac{l}{L} = \tau A \frac{L}{l}.$$

For a neo-Hookean model as a special case of Eq. (5) with $c_1 = \frac{1}{2}\mu$ and $c_2 = 0$, the free energy is

$$\psi = \frac{1}{2} \mu [\lambda^2 + 2/\lambda - 3],$$

and the Piola stress becomes

$$P = \mu [\lambda - 1/\lambda^2].$$

With the force F measured from microneedle deflection, and the stretch λ measured from videoscropy, the axonal stiffness follows directly as $\mu A = F/[\lambda - 1/\lambda^2]$.

2.1.2 Example: Lateral Tension Testing of Axons

Another popular technique is to attach a calibrated microneedle at the center of the axon and pull the axon laterally, orthogonal to its long axis (Dennerll, Joshi, Steel, Buxbaum, & Heidemann, 1988). Similar to the axial experiment, the applied force is calculated from the deformation of the calibrated needle and compared against the lateral deformation of the axon. Figure 3 illustrates the microneedle experiment with lateral axonal deformation.

The kinematics of the lateral microneedle experiment are defined through the scalar φ , the initial axonal length L , the deformed axonal length l with $(\frac{1}{2} l)^2 = (\frac{1}{2} L)^2 + \varphi^2$, the axonal stretch $\lambda = l/L$, and its derivative $d\lambda/d\varphi$,

$$l = [L^2 + 4\varphi^2]^{1/2} \quad \lambda = \frac{[L^2 + 4\varphi^2]^{1/2}}{L} \quad \frac{d\lambda}{d\varphi} = \frac{2}{Ll} \varphi.$$

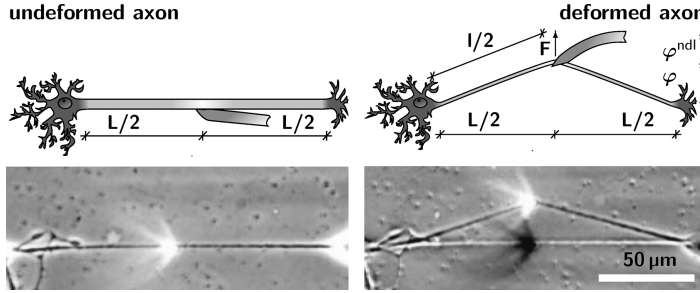


Figure 3 Microneedle experiment to probe the stiffness of single axons through controlled lateral deformation (Bernal, Pullarkat, & Melo, 2007). Undeformed axon of length L with the needle in contact at bright spot (left) and deformed axon of length l after lateral pulling with a needle force F (right).

For laterally pulled axons, the general force-deformation relation (14) reduces to the following expression,

$$F = 2PA \frac{\varphi}{l} = 2SA \frac{\varphi}{L} = 2\tau A \frac{L\varphi}{l^2}.$$

For a neo-Hookean model with $c_1 = \frac{1}{2}\mu$ and $c_2 = 0$, the free energy (5) is

$$\psi = \frac{1}{2}\mu [\lambda^2 + 2/\lambda - 3].$$

For small deformations, with $\lambda \rightarrow 1$, the Piola stress becomes a linear function of the stretch λ ,

$$P = \mu [\lambda - 1].$$

The axonal force-deformation relation takes the following expression,

$$\bar{F} = \frac{\mu A}{L} \Delta l + F_0 \quad \text{with} \quad \bar{F} = \frac{l}{2\varphi} F,$$

where $\mu A/L$ is the axial axonal stiffness and F_0 is the prestress.

Figure 4 illustrates the axonal force $\bar{F} = l/2 \varphi F$ versus the axonal elongation $\Delta l = L - l$ for three different axons with initial lengths of $L = 96, 176,$ and $52 \mu\text{m}$ (Dennerll et al., 1988). The slopes and intercepts are related to the axonal stiffness $\mu A/L$ and to the prestress F_0 . The lines illustrate the best fit of the parameter identification with axonal stiffnesses of $\mu A/L = 3.07 \times 10^{-4} \text{N/m}$, $1.75 \times 10^{-4} \text{N/m}$, and $0.90 \times 10^{-4} \text{N/m}$ and prestresses of $F_0 = 0.59, 0.48,$ and 0.38 nN for the circle, square, and diamond data sets.

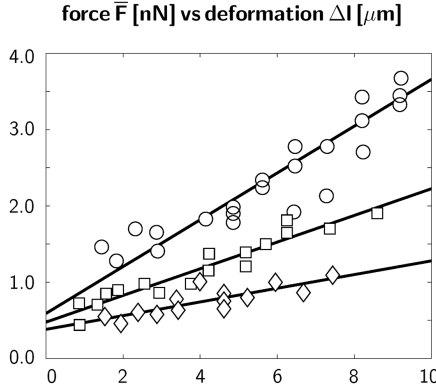


Figure 4 The axonal force \bar{F} increases linearly with axonal lengthening Δl . Circles, squares, and diamonds display forces for axons with different initial lengths of $L = 96, 176,$ and $52 \mu\text{m}$ (Dennerll et al., 1988). The slopes and intercepts are related to the axonal stiffness $\mu A/L$ and to the prestress F_0 . The lines illustrate the parameter identification with axonal stiffnesses of $\mu A/L = 3.07 \times 10^{-4} \text{ N/m}, 1.75 \times 10^{-4} \text{ N/m},$ and $0.90 \times 10^{-4} \text{ N/m}$ and prestresses of $F_0 = 0.59, 0.4,$ and 0.38 nN for the circle, square, and diamond data sets.

These three experiments are part of a large set of experiments with a total of 82 neurites. In all 82 neurites, the prestress varied over three orders of magnitude, but was always positive and clustered around values of $F_0 = 3.5^{-4} \text{ N}$. The mean axonal stiffness was $\mu A/L = 2.44 \pm 2.2 \times 10^{-4} \text{ N/m}$ (Dennerll et al., 1988).

For larger deformations, the experiments reveal a nonlinear behavior with respect to both strain and prestress (Bernal et al., 2007). We can capture this nonlinearity by a nonlinear constitutive model, e.g., of Saint Venant–Kirchhoff type, with

$$\psi = \frac{1}{8} \mathbf{E} [1 - \lambda^2]^2 = \frac{1}{2} E \mathbf{E} E,$$

where \mathbf{E} is Young's modulus and $E = \frac{1}{2} [\lambda^2 - 1] = 2 \varphi^2 / L^2$ is the Green–Lagrange strain. The Piola stress follows as

$$P = \frac{1}{2} \mathbf{E} [\lambda^2 - 1] \lambda = 2 E \frac{\varphi^2}{L^2} \lambda,$$

and the microneedle force–deformation relation becomes

$$F = 4 \mathbf{E} A \frac{\varphi^3}{L^3} + 2 F_0 \frac{\varphi}{L},$$

where EA is the axonal stiffness and F_0 is the prestress. This implies that the microneedle force F increases cubically with the relative deformation φ/L and linearly with the prestress F_0 .

Figure 5 illustrates the nonlinear increase in the microneedle force F with increasing relative deformation φ/L for three different axons (Bernal et al., 2007). The nonlinearity is related to the axial stiffness EA and the nonzero slope at the origin indicates the existence of prestress F_0 . The parameter identification reveals axial stiffnesses of $EA = 6.8, 2.1,$ and 3.6 nN and prestresses of $F_0 = 1.0, 0.2,$ and 0.0 nN for the diamond, square, and circular data sets. After dividing the axonal stiffness through the individual cross section area A , the axonal stiffness was relatively constant at $E = 12.2$ kPa (Bernal et al., 2007). Compared to the growth cone, which consists of loosely assembled actin filaments with a stiffness of $E = 0.1$ kPa, this suggests that axons, which are made of densely packed microtubules, are about two orders of magnitude stiffer under tensile loading.

Figure 6 illustrates the parameter sensitivity of the lateral microneedle experiment. The white circles display the force strain relation for a characteristic microneedle experiment with an axial stiffness of $EA = 6.8$ nN and a prestress of $F_0 = 1.0$ nN (Bernal et al., 2007). The nonlinearity is related to the axial stiffness EA and the nonzero slope at the origin indicates the existence of prestress F_0 . Increasing the axial stiffnesses EA cubically increases the

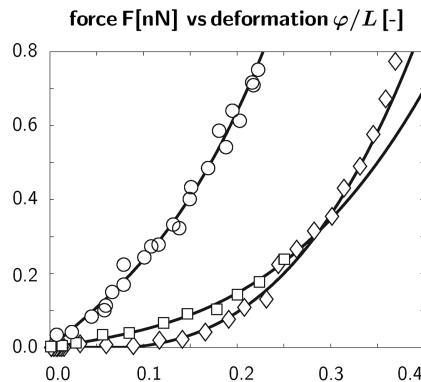


Figure 5 The needle force F increases nonlinearly with relative lateral deformation φ/L . Circles, squares, and diamonds display forces for different axons (Bernal et al., 2007). The nonlinear increase in force is related to the axial stiffness EA ; a nonzero slope at the origin indicates the existence of prestress S_0 . The curves result from the parameter identification with axial stiffnesses of $EA = 6.8, 2.1,$ and 3.6 nN and prestresses of $F_0 = 1.0, 0.2,$ and 0.0 nN for the circle, square, and diamond data sets.

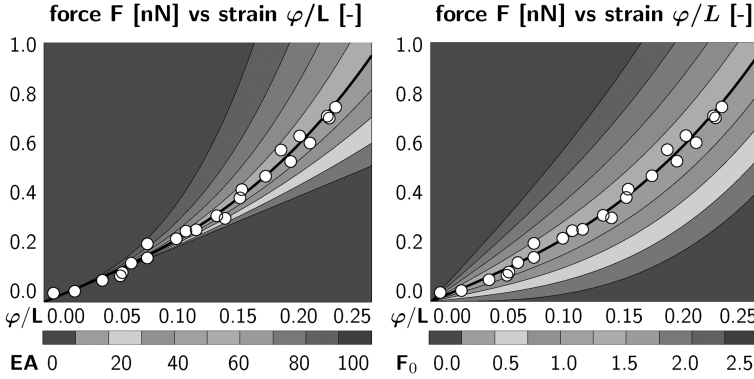


Figure 6 The needle force F increases nonlinearly with relative lateral deformation φ/L . Circles display forces for microneedle experiment (Bernal et al., 2007). The curves results from the parameter identification with an axial stiffness of $EA = 6.8$ nN and a prestress of $F_0 = 1.0$ nN. Increasing the axial stiffnesses EA cubically increases the microneedle force (left). Increasing the prestress F_0 linearly increases the microneedle force (right).

microneedle force. Increasing the prestress F_0 linearly increases the microneedle force.

2.2 Elasticity of Gray and White Matter Tissue

Brain tissue is extremely soft, and, not surprisingly, difficult to test experimentally and characterize mathematically (Goriely et al., 2015). Over short time scales, brain tissue is rate dependent; it behaves as a viscoelastically (Galford & McElhaney, 1969), or, depending on the clinical situation of interest, even poroviscoelastically (Franceschini, Bigoni, Regitnig, & Holzapfel, 2006). Over long time scales, brain tissue is commonly modeled as incompressible, hyperelastic material (Bilston, 2011). For the kinematic characterization, this implies that the deformation gradient \mathbf{F} is typically decomposed into a volumetric contribution, characterized through the Jacobian J , and an isochoric, volume-preserving contribution $\bar{\mathbf{F}}$,

$$\mathbf{F} = \nabla_{\mathbf{x}}\boldsymbol{\varphi} = J^{1/3}\bar{\mathbf{F}} \quad \text{with} \quad \bar{\mathbf{F}} = J^{-1/3}\mathbf{F}. \quad (15)$$

The left Cauchy Green deformation tensor \mathbf{b} obeys a similar decomposition, where $\bar{\mathbf{b}}$ denotes the isochoric part,

$$\mathbf{b} = \mathbf{F} \cdot \mathbf{F}^t = J^{2/3}\bar{\mathbf{b}} \quad \text{with} \quad \bar{\mathbf{b}} = \bar{\mathbf{F}} \cdot \bar{\mathbf{F}}^t. \quad (16)$$

We can then introduce the invariants,

$$\begin{aligned}
I_1 &= \operatorname{tr}(\mathbf{b}) = \lambda_1^2 + \lambda_2^2 + \lambda_3^2 \\
I_2 &= \frac{1}{2}[\operatorname{tr}^2(\mathbf{b}) - \operatorname{tr}(\mathbf{b}^2)] = \lambda_1^2\lambda_2^2 + \lambda_2^2\lambda_3^2 + \lambda_3^2\lambda_1^2 \\
J &= \det^{1/2}(\mathbf{b}) = \lambda_1 \lambda_2 \lambda_3,
\end{aligned} \tag{17}$$

their isochoric counterparts, $\bar{I}_1 = J^{-2/3}I_1$, $\bar{I}_2 = J^{-4/3}I_2$, and $\bar{I}_3 = 1$, and their derivatives,

$$\begin{aligned}
\partial I_1 / \partial \mathbf{F} &= 2\mathbf{F} & \partial I_1 / \partial \mathbf{b} &= \mathbf{I} \\
\partial I_2 / \partial \mathbf{F} &= 2I_1\mathbf{F} - \mathbf{F} \cdot \mathbf{F}^t \cdot \mathbf{F} & \partial I_2 / \partial \mathbf{b} &= I_1\mathbf{I} - \mathbf{b} \\
\partial J / \partial \mathbf{F} &= J\mathbf{F}^{-t} & \partial J / \partial \mathbf{b} &= \frac{1}{2}J\mathbf{b}^{-1},
\end{aligned} \tag{18}$$

where $I_3 = J^2$. Many common constitutive models for brain tissue are special cases of the general Ogden model (Ogden, 1972),

$$\psi = \sum_{p=0}^{\infty} \frac{1}{2m_p} \left[\lambda_1^{2m_p} + \lambda_2^{2m_p} + \lambda_3^{2m_p} - 3 \right] + U(J), \tag{19}$$

where c_p and m_p are material-specific parameters and the function $U(J)$ is related to the volumetric response. For the special case of the Mooney Rivlin model with $m_1 = 1$, $m_2 = -1$, and $2[c_1 + c_2] = \mu$, the free energy of the Ogden model (19) simplifies to $\psi = c_1 [\bar{I}_1 - 3] + c_2 [\bar{I}_2 - 3] + U(J)$, or, in terms of the principal stretches,

$$\psi = \frac{1}{2} c_1 [\lambda_1^2 + \lambda_2^2 + \lambda_3^2 - 3] + \frac{1}{2} c_2 [\lambda_1^{-2} + \lambda_2^{-2} + \lambda_3^{-2} - 3] + U(J). \tag{20}$$

For the special case of the neo-Hookean model with $m_1 = 1$, $2c_1 = \mu$, and $c_2 = 0$, the free energy (20) further simplifies to $\psi = c_1 [\bar{I}_1 - 3] + U(J)$, or, in terms of the principal stretches,

$$\psi = \frac{1}{2} c_1 [\lambda_1^2 + \lambda_2^2 + \lambda_3^2 - 3] + U(J). \tag{21}$$

The Piola stress for the Mooney Rivlin and neo-Hookean models follows from the Clausius Duhem inequality,

$$\mathbf{P} = \frac{\partial \psi}{\partial \mathbf{F}} = \frac{2}{J^{2/3}} [c_1 + \bar{I}_1 c_2] \mathbf{F} - \frac{2}{J^{4/3}} c_2 \mathbf{F} \cdot \mathbf{F}^t \cdot \mathbf{F} - \frac{2}{3} [\bar{I}_1 c_1 + 2\bar{I}_2 c_2] \mathbf{F}^{-t} - Jp\mathbf{F}^{-t}, \tag{22}$$

where $p = -\partial U / \partial J$. The Kirchhoff stress $\boldsymbol{\tau} = \mathbf{P} \cdot \mathbf{F}^t$ follows from its push forward,

$$\boldsymbol{\tau} = 2 \frac{\partial \psi}{\partial \mathbf{b}} \cdot \mathbf{b} = \frac{2}{J^{2/3}} [c_1 + \bar{I}_1 c_2] \mathbf{b} - \frac{2}{J^{4/3}} c_2 \mathbf{b}^2 - \frac{2}{3} [\bar{I}_1 c_1 + 2 \bar{I}_2 c_2] \mathbf{I} - J p \mathbf{I}, \quad (23)$$

In the case of incompressibility, with $J = 1$ and $\det(\mathbf{b}) = 1$, $p = p^*$ no longer follows from a constitutive equation. Instead, it becomes an arbitrary Lagrange multiplier associated with the incompressibility constraint, $J = 1$. In the case of incompressibility, we can apply the Cayley–Hamilton theorem, $\mathbf{b}^{-1} = \mathbf{b}^2 - I_1 \mathbf{b} + I_2 \mathbf{I}$, to obtain the frequently used Rivlin Ericksen representation of the stress (Mihai, Chin, Janmey, & Goriely, 2015),

$$\boldsymbol{\tau} = 2c_1 \mathbf{b} - 2c_2 \mathbf{b}^{-1} - p^* \mathbf{I} \quad \text{with} \quad p^* = Jp + \frac{2}{3} [I_1 c_1 - I_2 c_2]. \quad (24)$$

The material parameters c_1 and c_2 are phenomenological parameters, which we can identify through finite deformation experiments.

2.2.1 Example: Shear-Compression Testing of Brain Tissue

Historically, most experiments to characterize brain tissue have focused on a single load case, uniaxial tension (Miller & Chinzei, 2002), compression (Miller & Chinzei, 1997), or shear (Bilston et al., 2001), and fitted the material parameters to one particular loading scenario (Bilston, 2011). This implies that the reported tensile, compressive, and shear stiffnesses vary significantly, often by several orders of magnitude (Chatelin et al., 2010). Recent interest has turned towards characterizing the constitutive behavior of brain tissue under combined shear and axial loading (Pogoda et al., 2014).

Figure 7 compares the performance of the neo-Hookean, Mooney Rivlin, and Ogden models (Mihai et al., 2015) with combined shear-compression experiments of adult mouse brain tissue (Pogoda et al., 2014). The experiments at 2% shear, superposed to 40% compression and tension, reveal the extreme shear sensitivity to axial loading. The shear modulus μ increases by a factor three in compression and by a factor two in tension. The diamond, triangle, and square curves illustrate the parameter identification of the neo-Hookean model with $c_1 = 191.45$, the Mooney Rivlin model with $c_1 = 0.45$ and $c_2 = 191$, and the fourth-order Ogden model with $c_1 = -3236$, $c_2 = -2197$, $c_3 = 896$, $c_4 = 265$ and exponents $m_1 = 1$, $m_2 = -1$, $m_3 = 2$, and $m_4 = -2$ (Mihai et al., 2015). The comparison of the three curves underlines the linear behavior of the neo-Hookean model, the moderately deformation-dependent behavior of the Mooney–Rivlin model, and the extremely deformation-dependent behavior of the Ogden model (Ogden, 1972). Of these three, only the Ogden

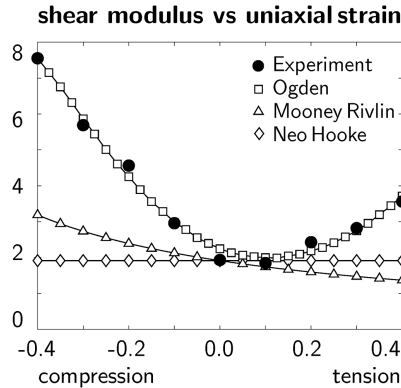


Figure 7 Shear sensitivity of brain tissue. The shear modulus μ increases with increasing axial loading. Solid circles summarize the experimentally measured shear sensitivity at 2% shear superposed to 40% compression and tension (Pogoda et al., 2014). Diamonds, triangles, and squares indicate the best fit of the neo-Hookean, Mooney Rivlin, and Ogden models.

model is truly capable of reproducing the characteristic shear sensitivity of brain tissue. However, this example also reveals a major deficiency of the Ogden model: While its parameters allow a systematic fit of an arbitrary loading curve, they lack a profound mechanistic interpretation. This suggests to link the material properties of brain tissue to the underlying microstructure (Cloots, van Dommelen, Nyberg, Kleiven, & Geers, 2011), and create hierarchical models that integrate the axon-level measurements from the previous Section 2.1 into a hierarchical constitutive model. The individual axon orientation would then inherently introduce brain tissue anisotropy (Holland, Miller, & Kuhl, 2015).

2.3 Elasticity of the Brain

Despite intense efforts toward understanding the mechanical properties of brain tissue as a whole, the rheological differences between gray and white matter tissue remain poorly characterized. Reported stiffness contrasts differ by an order of magnitude and more, mainly because of inconsistencies in sample preparation, postmortem timing, and testing conditions (Chatelin et al., 2010). The individual stiffnesses of gray and white matter play a critical role in human brain morphogenesis: Physics-based modeling predicts that the gyral wavelength increases with the third root of the stiffness ratio between gray and white matter (Allen, 1969); yet, this ratio is subject of ongoing discussion (Budday, Steinmann, & Kuhl, 2015a).

At the tissue level, mechanical indentation tests suggest that gray matter is about one third softer than white matter, 1.8 kPa versus 1.2 kPa (Kaster, Sack, & Samani, 2011) and 2 kPa versus 3 kPa (van Dommelen, van der Sande, Hrapko, & Peters, 2010) for porcine brain and 1.9 kPa versus 1.4 kPa for bovine brain (Budday et al., 2014). At the cellular level, scanning force microscopy suggests the opposite with gray matter about twice as stiff as white matter, on the order of 100 Pa versus 50 Pa for ultra thin mouse spinal cord slices (Koser, Moendarbary, Hanne, Kuerten, & Franze, 2015) and 500 Pa versus 250 Pa for rat cerebellum slices (Christ et al., 2010). Discrepancies in these measurements not only reflect the extreme strain rate sensitivity of brain tissue, but also its nonlinear behavior and its compression stiffening (Pogoda et al., 2014). *In vivo*, magnetic resonance elastography suggests that mature gray and white matter shear stiffnesses are rather indistinguishable, on the order of 3.14 ± 0.27 kPa versus 3.07 ± 0.28 kPa in ferrets (Feng, Clayton, Chang, Okamoto, & Bayly, 2013), and 3.1 ± 0.1 kPa versus 2.7 ± 0.1 kPa in humans (Green, Bilston, & Sinkus, 2008).

2.3.1 Example: Indentation of Gray and White Matter Tissue

A popular method to characterize the individual stiffnesses of gray and white matter tissue is indentation testing. Figure 8 displays a typical test setup for gray and white matter indentation in a freshly harvested brain slice. When kept intact and hydrated, thick brain slices can be preserved over periods of days without significant alteration in mechanical properties (Budday et al., 2014). An inherent advantage of testing thick, structurally intact brain slices, rather than small cylindrical (Franceschini et al., 2006), disc-shaped (Pervin & Chen, 2009) or cuboid (Prange & Margulies, 2002) specimens, is that larger structural dimensions naturally minimize dehydration, swelling, structural degradation, and boundary effects (Miller, 2011). In a typical



Figure 8 Indentation testing of white and gray matter tissue to characterize the stiffness contrast (Budday et al., 2014). Fresh bovine brain (left), brain slice mounted in indentation apparatus (middle), and displayed in the dish (right).

indentation experiment, the contact stiffness k is the average slope of the force–depth curve. In soft matter indentation, to minimize the influence of adhesion, it seems reasonable to neglect the first half of this curve, and average the contact stiffness only over the second half of the loading curve. The effective elastic modulus E_{eff} of the indent then follows directly from the standard relation (Oliver & Pharr, 2004),

$$E_{\text{eff}} = \frac{\sqrt{\pi}k}{2\sqrt{A}}, \quad (25)$$

where A is the projected contact area underneath the indenter. For a circular flat punch, the contact area, $A = 1/4 \pi d^2$, is independent of the indentation depth, and the elastic modulus simplifies to the following expression,

$$E_{\text{eff}} = k/d. \quad (26)$$

Since brain tissue is significantly softer than the indenter tip, the indenter deformation is negligible, and the tissue stiffness E follows directly from the effective stiffness E_{eff} and Poisson’s ratio ν ,

$$E = [1 - \nu^2] E_{\text{eff}}. \quad (27)$$

With the common assumption of incompressibility, $\nu = 0.5$, the elastic tissue stiffness take the following simple expression,

$$E = \frac{3}{4} k/d. \quad (28)$$

This implies that the gray and white matter moduli are directly proportional to the contact stiffness k and inversely proportional to the punch diameter d .

Figure 9 displays characteristic indentation curves of white and gray matter tissue. In this displacement–controlled experiment on thick brain slices, white matter, with a modulus of 1.9 kPa, was on average 36% stiffer than gray matter, with a modulus of 1.4 kPa. This stiffness difference is micro-structurally plausible since white matter consists primarily of myelinated axons, which act as a network of biopolymer filaments, while gray matter is largely composed of cell bodies (Alberts et al., 2014). During brain development, however, when axons are not yet myelinated, this stiffness ratio could be reversed, which might explain the experimental discrepancies (Koser et al., 2015) and the stiffness contrasts required for brain morphogenesis (Budday, Kuhl, & Hutchinson, 2015). We discuss the mechanics of neurodevelopment in the following section.

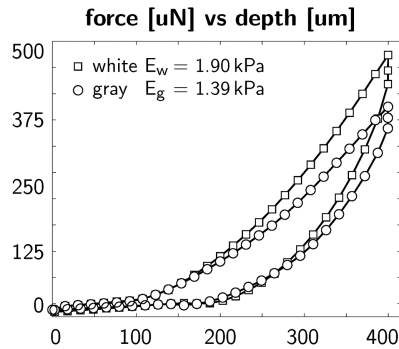
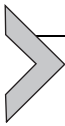


Figure 9 Indentation testing of white and gray matter tissue to characterize the stiffness contrast. In displacement-controlled loading, holding, unloading experiments, white matter was on average one third stiffer than gray matter (Budday et al., 2014). Both tissues display a viscous response as the forces relax during the holding phase.



3. NEURODEVELOPMENT

Under large deformations, over long time scales, our brain becomes inelastic and capable of adapting to environmental cues. In this section, we focus on the inelasticity associated with neurodevelopment. We restrict our attention to phenomena on relatively slow time scales, at which the brain is able to sense, respond to, and adapt to changes in its environment. We collectively refer to these phenomena as growth. While many environmental conditions may impact the brain during neurodevelopment, here we focus primarily on the brain as a growing solid and neglect its interactions with the skull, the ventricles, and the cerebrospinal fluid. We highlight the growth of single neurons in Section 3.1, the growth of gray and white matter tissue in Section 3.2, and the growth of the brain in Section 3.3. Similar to the previous section, we complement the theory with experiments, illustrate what we can learn from these experiments, and discuss how the findings on the individual scales add to our overall understanding of the brain as a whole.

3.1 Growth of Single Neurons

During early development, axons grow in length to form connections between different regions of the brain (Pfister, Iwata, Meaney, & Smith, 2004). As those regions move closer together or further apart, axons experience what has been termed towed growth, a chronic lengthening or

shortening to maintain a desired level of axonal tension (Bray, 1984; Dennerll et al., 1989). To characterize the kinematics of axonal growth, we multiplicatively decompose the total axonal stretch λ , the ratio of the unstretched axonal length L and the stretched axonal length l , into an elastic and a growth part,

$$\lambda = l / L = \lambda^e \lambda^g. \quad (29)$$

Growth theories commonly assume that only the elastic deformation causes stress. We use the Mooney Rivlin model from equation (2), but now parameterized only in terms of the elastic part of the deformation,

$$\psi = c_1 [I_1^e - 3] + c_2 [I_2^e - 3], \quad (30)$$

where I_1^e and I_2^e are elastic invariants in terms of elastic stretches $\lambda_1^e, \lambda_2^e, \lambda_3^e$. In the case of elastic incompressibility, $J^e = \lambda_1^e \lambda_2^e \lambda_3^e \doteq 1$, and uniaxial tension $\lambda_1^e = \lambda^e$ and $\lambda_2^e = \lambda_3^e = 1/(\lambda^e)^{1/2}$, the elastic invariants become a function of the elastic stretch λ^e introduced in Eq. (29),

$$I_1^e = (\lambda^e)^2 + \frac{2}{\lambda^e} \quad I_2^e = 2\lambda^e + \frac{1}{(\lambda^e)^2} \quad I_3^e = 1, \quad (31)$$

and the Mooney Rivlin free energy reduces to the following expression,

$$\psi(\lambda^e) = c_1 \left[(\lambda^e)^2 + \frac{2}{\lambda^e} - 3 \right] + c_2 \left[2\lambda^e + \frac{1}{(\lambda^e)^2} - 3 \right]. \quad (32)$$

It proves convenient to reparameterize the free energy in terms of the total axonal stretch λ and the axonal growth λ^g ,

$$\psi(\lambda, \lambda^g) = c_1 \left[\frac{\lambda^2}{(\lambda^g)^2} + 2\frac{\lambda^g}{\lambda} - 3 \right] + c_2 \left[2\frac{\lambda}{\lambda^g} + \frac{(\lambda^g)^2}{\lambda^2} - 3 \right]. \quad (33)$$

From Clausius Duhem inequality, we can then derive the Piola stress P , either parameterized in terms of the elastic stretch λ^e ,

$$P = \frac{\partial \psi}{\partial \lambda} = \frac{\partial \psi}{\partial \lambda^e} \frac{\partial \lambda^e}{\partial \lambda} = \frac{1}{\lambda^g} P^e \quad P^e = \frac{\partial \psi}{\partial \lambda^e} = 2 \left[c_1 + c_2 \frac{1}{\lambda^e} \right] \left[\lambda^e - \frac{1}{(\lambda^e)^2} \right], \quad (34)$$

or in terms of the total axonal stretch λ and the axonal growth λ^g ,

$$P = \frac{\partial \psi}{\partial \lambda} = \frac{2}{\lambda^g} \left[c_1 + c_2 \frac{\lambda^g}{\lambda} \right] \left[\frac{\lambda}{\lambda^g} - \frac{(\lambda^g)^2}{\lambda^2} \right]. \quad (35)$$

Its pull back introduces the Piola Kirchhoff stress $S = \lambda^{-1}P$,

$$S = 2 \frac{\partial \psi}{\partial C} = 2 \frac{\partial \psi}{\partial \lambda^e} \frac{\partial \lambda^e}{\partial C^e} \frac{\partial C^e}{\partial C} = \frac{1}{\lambda} P = \frac{2}{(\lambda^g)^2} \left[c_1 + c_2 \frac{1}{\lambda^e} \right] \left[1 - \frac{1}{(\lambda^e)^3} \right], \quad (36)$$

its push forward introduces the Kirchhoff stress $\tau = P\lambda$,

$$\tau = 2 \frac{\partial \psi}{\partial b} b = 2 \frac{\partial \psi}{\partial \lambda^e} \frac{\partial \lambda^e}{\partial b^e} \frac{\partial b^e}{\partial b} b = P\lambda = 2 \left[c_1 + c_2 \frac{1}{\lambda^e} \right] \left[(\lambda^e)^2 - \frac{1}{\lambda^e} \right]. \quad (37)$$

The equilibrium equation uses the total stress P and remains unaffected by growth. Similar to the purely elastic case, it yields a direct relation between the external force F and the internal axonal stress P through Eq. (14),

$$F = PAL \frac{d\lambda}{d\varphi}. \quad (38)$$

Similar to Section 2.1, the derivative $d\lambda/d\varphi$, depends on the experimental setup, either axial or lateral tension, with

$$F^{\text{axl}} = PA \quad \text{and} \quad F^{\text{lat}} = 2PA \varphi/l. \quad (39)$$

To close the set of equations, we need to constitutively define the growth kinetics, the functional form by which the axon responds to deformation. We suggest the following stretch-driven growth kinetics,

$$\dot{\lambda}^g = k(\lambda^g) \phi(\lambda, \lambda^g), \quad (40)$$

where k is a function to possibly limit growth to a maximum value λ^{max} and ϕ is a growth criterion that activates growth only if the elastic stretch λ^e exceeds a critical limit λ^{crit} (Zöllner, Abilez, Böl, & Kuhl, 2012),

$$k = \frac{1}{\tau} \left[\frac{\lambda^{\text{max}} - \lambda^g}{\lambda^{\text{max}} - 1} \right]^\gamma \quad \text{and} \quad \phi = \left\langle \frac{\lambda}{\lambda^g} - \lambda^{\text{crit}} \right\rangle = \langle \lambda^e - \lambda^{\text{crit}} \rangle. \quad (41)$$

The term in the Macaulay brackets is $\langle \lambda^e - \lambda^{\text{crit}} \rangle = \lambda^e - \lambda^{\text{crit}}$ if $\lambda^e \geq \lambda^{\text{crit}}$ and zero otherwise. Experimental evidence suggests that axons can be stretched to multiples of their original length (Pfister et al., 2004). This implies that axonal growth is unlimited, $\lambda^{\text{max}} \rightarrow \infty$, that the term in the brackets converges to one, $[\lambda^{\text{max}} - \lambda^g]/[\lambda^{\text{max}} - 1] \rightarrow 1$, and that the exponent γ can

simply be chosen to one, $\gamma = 1$. The scaling function k then reduces to $k = 1/\tau = G^{\text{axn}}$, where G^{axn} is the axonal growth rate (Holland et al., 2015).

3.1.1 Example: Growing Neurites, Force and Length

Towed growth has been extensively studied over the past two decades for either axons or neurites (Bray, 1984; Lamoureux, Heidemann, & E., 2011; O'Toole, Lamoureux, & Miller, 2008). Figure 10 illustrates the microneedle experiment of towed growth with lateral deformation. In most experiments of displacement-controlled towed growth, the stretch is applied in a single step, and then held constant throughout the duration of the experiment,

$$\lambda = l/L = \lambda^e \lambda^g = \text{const.} \quad \text{and} \quad \dot{\lambda} = \dot{\lambda}^e \dot{\lambda}^g = 0.$$

Initially, the axon or neurite is ungrown and its entire deformation is elastic,

$$\lambda_0^g = 1 \quad \text{and} \quad \lambda_0^e = \lambda.$$

Over time, the neurite grows and the elastic stretch relaxes back to its baseline value,

$$\dot{\lambda}^g = G^{\text{axn}} \langle \lambda^e - \lambda^{\text{crit}} \rangle \quad \text{and} \quad \dot{\lambda}^e = -G^{\text{axn}} \langle \lambda^e - \lambda^{\text{crit}} \rangle.$$

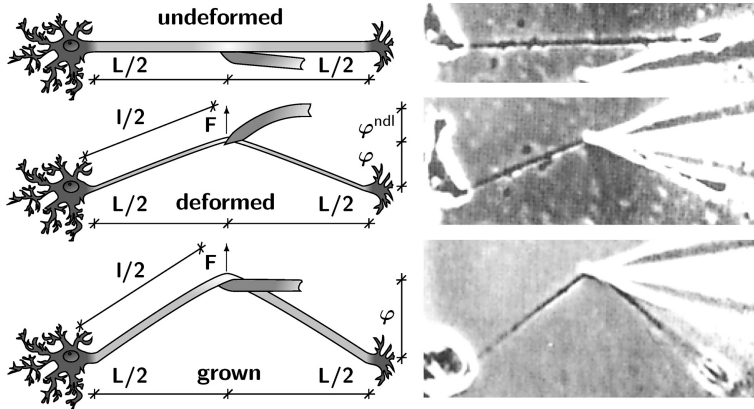


Figure 10 Microneedle experiment to probe the towed growth of single neurites through controlled lateral deformation (Dennerll et al., 1989). Undeformed neurite of length L with the needle approaching the neurite (top), deformed neurite of length l immediately after lateral pulling with a needle force F (middle), and grown neurite of new length l after growing in response to a lateral needle force F (bottom).

Toward the end of the growth process, at biological equilibrium, the total stretch has translated into growth, and the elastic stretch has returned to its homeostatic equilibrium value,

$$\lambda_{\infty}^g = \lambda \quad \text{and} \quad \lambda_{\infty}^e = 1.$$

The neurite force F reflects the behavior of the elastic stretch λ^e : It increases initially to $F(\lambda_0^e) = F(\lambda)$, and then gradually relaxes back to its physiological value $F(\lambda_{\infty}^e) = F_0$.

Figure 11 illustrates the temporal evolution of the force F and length l in a single-step displacement controlled microneedle experiment with PC12 neurites (Dennerll et al., 1989). The total length $\bar{l} = l + \Delta l^{\text{ndl}}$, the sum of the neurite length l and the deflection of the pulling microneedle Δl^{ndl} , is generated in a single step and then held constant. The microneedle deflection Δl^{ndl} is measured videoscopically. It increases initially, but then gradually relaxes over time. The external microneedle force, which can be calculated directly from the microneedle deflection Δl^{ndl} , is in equilibrium with the internal neurite force F , which increases initially and then relaxes. At the same time, the neurite length l increases initially and then gradually creeps over time. The circles in Fig. 11 illustrate the force F and length l for a representative microneedle experiment (Dennerll et al., 1989). The solid lines represent the simulation with unlimited growth, $\dot{\lambda}^g = G^{\text{axn}} \langle \lambda^e - \lambda^{\text{crit}} \rangle$,

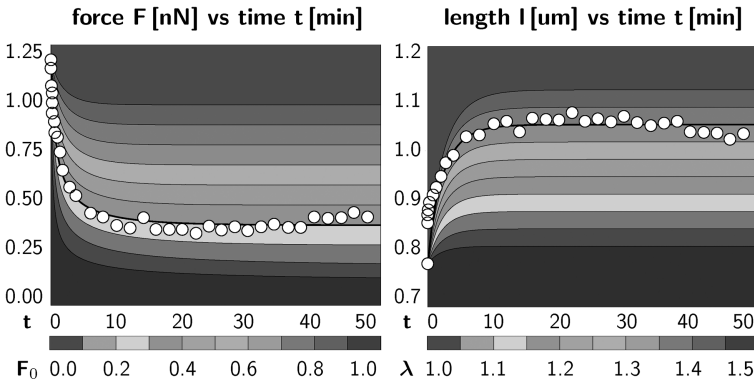


Figure 11 The force F upon a single lateral displacement increases initially but then gradually relaxes over time (left). The length l increases initially and then gradually creeps over time (right). Circles display the forces and lengths for a representative microneedle experiment with PC12 neurites (Dennerll et al., 1989). The curve results from the parameter identification with unlimited stretch-driven growth at a growth rate of $G^{\text{axn}} = 0.5/\text{min}$.

immediately upon stretch, $\lambda^{\text{crit}} = 1$. The best-fit growth rate for this experiment is $G^{\text{axn}} = 0.5/\text{min}$.

3.1.2 Example: Growing Axons, Axial and Transverse Stretch

From a thermodynamic point of view, the growing axon acts like an open system (Kuhl & Steinmann, 2003), which gradually adds mass along its length to reduce the axial stress and recover its homeostatic equilibrium state. A powerful method to quantify the amount of growth through the addition of new material is to monitor the transverse dimension of the axon (Lamoureux et al., 2010). Figure 12 illustrates the microneedle experiment of towed axial growth (Dennerll et al., 1989) to characterize gradual axonal growth.

The axial stretch λ^{\parallel} consists of an elastic contribution and axial growth,

$$\lambda^{\parallel} = \lambda^e \lambda^g = \lambda.$$

With elastic incompressibility, $J^e \doteq 1$, and no growth in thickness direction, the transverse stretch λ^{\perp} is directly related to the elastic stretch λ^e ,

$$\lambda^{\perp} = 1/(\lambda^e)^{1/2}.$$

Initially, the axon is ungrown, $\lambda_0^g = 1$, the entire axial deformation is elastic $\lambda_0^e = \lambda$, and the transverse stretch decreases to accommodate for the axial lengthening, $\lambda_0^{\perp} = 1/\lambda^{1/2}$. Over time, the axon grows, $\dot{\lambda}^g = G^{\text{axn}} \langle \lambda^e - \lambda^{\text{crit}} \rangle$, until the total stretch is accommodated by growth, $\lambda_{\infty}^g = \lambda$, the elastic

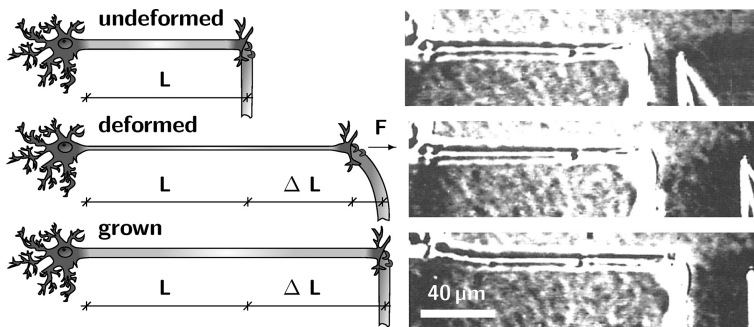


Figure 12 Microneedle experiment to probe the towed growth of single neurites through controlled axial deformation (Dennerll et al., 1989). Undeformed neurite of length L with the needle attached to the growth cone (top), deformed neurite of length $L + \Delta L$ with reduced thickness immediately after axial pulling with a needle force F (middle), and grown neurite of new length $L + \Delta L$ with recovered initial thickness (bottom).

deformation is relaxed back to its baseline value, $\lambda_\infty^e = 1$, and the transverse stretch recovers its initial value $\lambda_\infty^\perp = 1$.

Figure 13 shows an experiment of towed growth with displacement-controlled axonal elongation (Lamoureux et al., 2010). The top graphs summarize the applied axial stretch λ^\parallel versus the stretching time t for $n = 23$ individual chick sensory neurons, which were stretched to $\lambda = 1.3$ – 7.8 over a period of 1–10 h, and allowed to recover at that new length for 1–20 h. The bottom graphs summarize the resulting transverse stretch λ^\perp versus time t . The black dots indicate the experimental measurements at discrete points in time. The curves represent the computational simulations with the best-fit axonal growth rate of $G^{\text{axn}} = 0.08$ per h.

Figure 14 illustrates the temporal evolution of the transverse stretch λ^\perp and the volume growth $\lambda^\parallel \lambda^{\perp 2}$ versus time t for the calibrated growth rate of $G^{\text{axn}} = 0.08$ per h. The transverse stretch, λ^\perp , the relative change in axonal

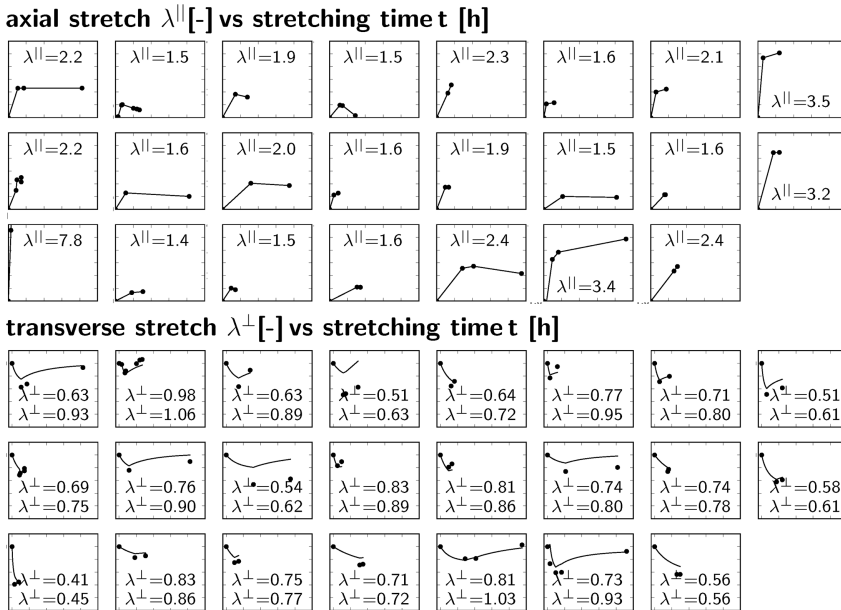


Figure 13 Towed growth of single axons. Axial stretch–time curves for 23 axons summarize the individual loading histories (top). Transverse stretch–time curves for 23 axons summarize the individual growth response to loading–holding experiments (bottom). Black dots indicate experimental measurements (Lamoureux et al., 2010). Curves represent computational simulations with an axonal growth rate of $G^{\text{axn}} = 0.08$ per h (Holland et al., 2015). Stretching times range from t 0 to 25 h, axial stretches λ^\parallel from 1.0 to 4.0, and transverse stretches λ^\perp from 0.0 to 1.0.

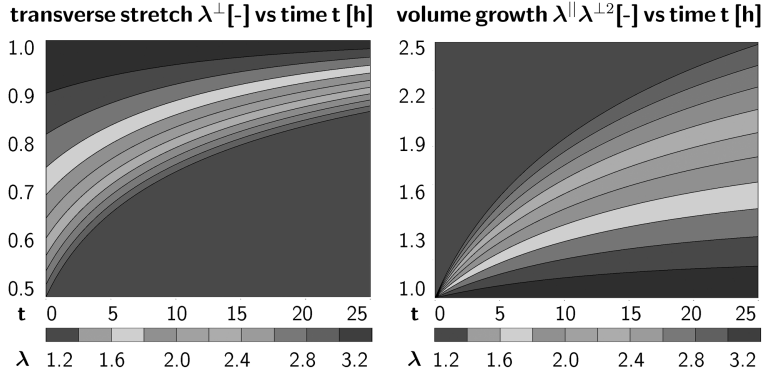


Figure 14 Transverse stretch λ^\perp and axial growth $\lambda^\parallel = (\lambda^\perp)^2 \lambda^\parallel$ for varying stretches λ with calibrated growth rate $G^{\text{axn}} = 0.08$ per h. The transverse stretch decreases initially and then gradually returns to its baseline value. The axonal growth increases gradually as the axon thickens.

thickness, decreases initially and then gradually returns to its baseline value of 1.0. The volume growth, $\lambda^\parallel \lambda^{\perp 2}$, the relative change in axonal volume, increases gradually as the axon thickens. Early experiments even suggest that towed axons rethicken beyond their initial thickness, i.e., $\lambda^\perp > 1$ (Bray, 1984).

3.2 Growth of Gray and White Matter Tissue

On the tissue scale, axonal growth translates into an increase of white matter volume. White matter tissue is surrounded by a cortical layer of gray matter, which also expands and grows, however, at a different rate (Raybaud, Ahmad, Rastegar, Shroff, & Al Nassar, 2013). Initially, the cortical layer is flat and the brain surface is smooth. In humans, at week 23 post gestation, the cortical layer begins to fold and introduces the characteristic wrinkled appearance with pronounced gyri and sulci (Budday, Steinmann, & Kuhl, 2015a). To establish analytical estimates for the evolving brain surface morphology, several groups have proposed to approximate cortical folding as the instability problem of a confined, layered medium subjected to growth-induced compression (Bayly, Taber, & Kroenke, 2014). This approximation uses the Föppl–von-Kármán theory (Föppl, 1907; von Kármán, 2010), and models the cortical deflection w with a classical fourth order plate equation (Dervaux, Ciarletta, & Ben Amar, 2009),

$$\mu_g \frac{t_g^3}{3} \frac{d^4 w}{dx^4} + P t_g \frac{d^2 w}{dx^2} = q. \quad (42)$$

Figure 15 illustrates the analytical model for cortical folding with the incompressible gray and white matter stiffnesses μ_g and μ_w , the cortical thickness t_g , the cortical pressure P , the cortical deflection w , and the deflection-induced transverse force q of the white matter foundation. A common approach is to adopt a sinusoidal ansatz for the cortical deflection w and for the transverse force q as a Maxwell-type viscoelastic response to deflection w (Bayly, Okamoto, Xu, Shi, & Taber, 2013),

$$\dot{q}_0 + G_w q_0 = -\mu_w n \dot{w}_0, \quad (43)$$

where G_w is the white matter growth rate. With the time operator G as the characteristic time scale of cortical folding and the correspondence principle, $\dot{q}_0 = G q_0$ and $\dot{w}_0 = G w_0$, we obtain the following explicit representations for the cortical deflection w and the transverse force q ,

$$\begin{aligned} w &= w_0 \cos(nx) \text{ with } n = \frac{2\pi/\lambda^{\text{crit}}}{G} \\ q &= q_0 \cos(nx) \text{ with } q_0 = -2\mu_w \frac{G}{G + G_w} n w_0. \end{aligned} \quad (44)$$

Here, w_0 is the amplitude of the deflection, q_0 is the amplitude of the force, n is the wavenumber, and λ is the gyral wavelength. Inserting this ansatz into

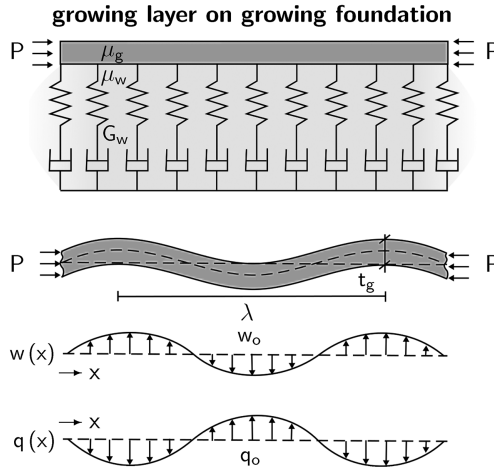


Figure 15 Analytical model of confined, layered medium subjected to growth-induced compression. The classical fourth order Föppl–von-Kármán plate theory provides analytical estimates for the gyral wavelength λ^{crit} in terms of the gray matter thickness t_g , the gray and white matter stiffnesses E_g and E_w , and the gray and white matter growth rates G_g and G_w .

the Föppl–von-Kármán plate Eq. (42) yields an equation for the cortical pressure P in terms of the wavenumber n ,

$$P(n) = \frac{1}{3} \mu_g t_g^2 n^2 + 2 \mu_w \frac{G}{G + G_w} \frac{1}{t_g n}. \quad (45)$$

The minimization problem, $P(n) \rightarrow \min$, with

$$\frac{dP}{dn} = \frac{2}{3} \mu_g t_g^2 n - 2 \mu_w \frac{G}{G + G_w} \frac{1}{t_g n^2} \stackrel{!}{=} 0 \quad (46)$$

defines the critical wavenumber n (Biot, 1957),

$$n = \frac{1}{t_g} \sqrt[3]{3 \frac{\mu_w}{\mu_g} \frac{G}{G + G_w}}. \quad (47)$$

With this wavenumber, the estimates for the critical pressure P^{crit} at the onset of folding (45),

$$P^{\text{crit}} = 3 \mu_w \frac{G}{G + G_w} \sqrt[3]{\frac{\mu_g}{3 \mu_w} \frac{G + G_w}{G}}, \quad (48)$$

and the critical wavelength (44),

$$\lambda^{\text{crit}} = 2 \pi t_g \sqrt[3]{\frac{\mu_g}{3 \mu_w} \frac{G + G_w}{G}}, \quad (49)$$

reveal that the critical wavelength, the distance between two neighboring gyri, is directly proportional to the cortical thickness t_g , the third root of the stiffness ratio μ_g/μ_w , and the inverse growth ratio G_w/G ,

$$\lambda^{\text{crit}} \propto t_g \quad \lambda^{\text{crit}} \propto \sqrt[3]{\mu_g/\mu_w} \quad \lambda^{\text{crit}} \propto \sqrt[3]{(1 + G_w/G)}. \quad (50)$$

For time constants $G \gg G_w$, white matter behaves like an elastic solid with a critical wavelength $\lambda^{\text{crit}} = 2 \pi t_g (\mu_g/(3\mu_w))^{1/3}$; for $G \ll G_w$, it behaves like a viscous fluid with $\lambda^{\text{crit}} \rightarrow \infty$. Large enough white matter growth rates, $G_w \gg G$, are even capable of suppressing cortical folding entirely.

3.2.1 Example: Morphogenesis and Gyral Wavelength

Figure 16 illustrates the critical wavelength λ^{crit} for varying stiffness ratios μ_g/μ_w and varying cortical thicknesses t_g , left, and for varying growth ratios G_w/G and varying cortical thicknesses t_g , right. The graphs visualize the

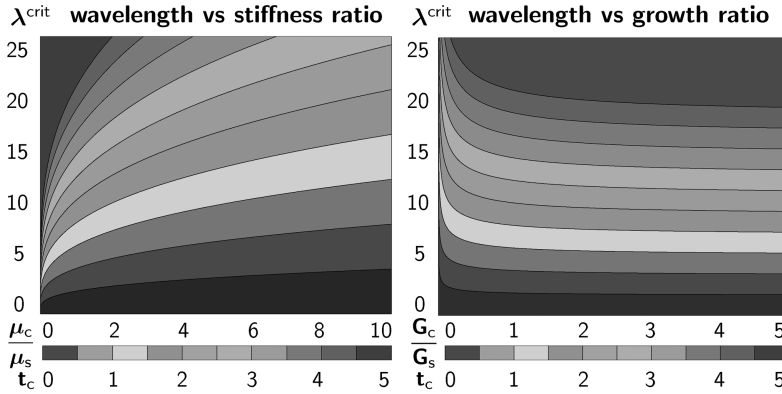


Figure 16 Critical wavelength λ^{crit} for varying stiffness ratios μ_g/μ_w and varying cortical thicknesses t_g (left) and for varying growth ratios G_g/G_w and varying cortical thickness t_g (right). The wavelength λ^{crit} increases with increasing cortical stiffness μ_g , with increasing subcortical growth rate G_w , and with increasing cortical thickness t_g .

analytical estimates: The wavelength increases linearly with increasing cortical thickness t_g , increases with increasing stiffness ratio μ_g/μ_w , and decreases with increasing growth ratio G_g/G_w .

Analytical modeling provides useful first estimates for the critical wavelength at the onset of folding. Yet, it fails to predict the evolution of complex folding morphologies beyond this first instability point (Ciarletta, Balbi, & Kuhl, 2014). Figure 17 illustrates the emerging instability pattern of a growing gray matter layer on a growing white matter foundation (Budday, Kuhl, & Hutchinson, 2015). The first row illustrates moderate growth beyond the first instability point with its characteristic symmetric, sinusoidal wrinkling patterns. The second row shows that further growth triggers symmetry breaking into nonsymmetric patterns with sharper sulci and smoother gyri. The third and fourth rows indicate that continuing growth beyond a second instability point induces period-doubling or period-tripling with alternating increasing and decreasing amplitudes (Budday, Steinmann, & Kuhl, 2015b). These simulations are highly nonlinear and require the continuum modeling of finite growth paired with computational solution strategies.

3.3 Growth of the Brain

To model cortical folding on arbitrary geometries, before and beyond the first instability point, we can generalize the one-dimensional growth of individual neurons to the three-dimensional theory of finite growth



Figure 17 Emerging instability patterns of primary and secondary bifurcations. Moderate growth beyond the first instability point creates a symmetric, sinusoidal wrinkling pattern. Further growth triggers symmetry breaking into a nonsymmetric pattern with sharper valleys and smoother ridges. Continuing growth beyond a second instability point initiates period doubling or period tripling with increasing and decreasing amplitudes (Budday, Kuhl, & Hutchinson, 2015).

(Ambrosi et al., 2011). To characterize finite deformations, we introduce the deformation map $\boldsymbol{\varphi}$, and adopt the concept of fictitious, incompatible configurations, associated with the multiplicative decomposition of the deformation gradient, $\mathbf{F} = \nabla_{\mathbf{x}}\boldsymbol{\varphi}$, into an elastic part \mathbf{F}^e and a growth part \mathbf{F}^g (Rodriguez, Hoger, & McCulloch, 1994),

$$\mathbf{F} = \nabla_{\mathbf{x}}\boldsymbol{\varphi} = \mathbf{F}^e \cdot \mathbf{F}^g. \quad (51)$$

The Jacobian of the deformation gradient defines the total change in tissue volume,

$$J = \det(\mathbf{F}) = J^e J^g, \quad (52)$$

which consists of an elastic volume change, $J^e = \det(\mathbf{F}^e)$, and a volume change related to growth $J^g = \det(\mathbf{F}^g)$. The incompatibility of growth implies that unlike the deformation gradient itself, neither the elastic tensor \mathbf{F}^e nor the growth tensor \mathbf{F}^g are gradients of a vector field. Instead, we have to prescribe the growth tensor constitutively and then determine the elastic tensor, $\mathbf{F}^e = \mathbf{F} \cdot \mathbf{F}^{g^{-1}}$ (BenAmar & Goriely, 2005). Only the elastic tensor \mathbf{F}^e enters the free energy function and induces stress. We can, for example, choose a Mooney Rivlin free energy function for both gray and white matter tissue (20), and parameterize it in terms of the elastic left Cauchy Green tensor, $\mathbf{b}^e = \mathbf{F}^e \cdot \mathbf{F}^{e^t}$, and the elastic Jacobian J^e ,

$$\psi = c_1 [I_1^e - 3] + c_2 [I_2^e - 3] + U(J^e), \quad (53)$$

where c_1 and c_2 are Mooney Rivlin parameters (Mooney, 1940; Rivlin, 1948). For the volumetric function $U(J^e)$, we can, e.g., use the following expression,

$$U = d_1 \ln^2(J^e) + d_2 \ln(J^e) \quad \text{with} \quad \frac{\partial U}{\partial J^e} = \frac{1}{J^e} [2d_1 \ln(J^e) + d_2]. \quad (54)$$

The Kirchhoff stress $\boldsymbol{\tau}$ follows from the standard Coleman–Noll evaluation of the dissipation inequality in open system thermodynamics (Göktepe, Abilez, & Kuhl, 2010),

$$\boldsymbol{\tau} = 2 \frac{\partial \psi}{\partial \mathbf{b}^e} \cdot \mathbf{b}^e = 2 [c_1 + c_2 I_1^e] \mathbf{b}^e - 2c_2 (\mathbf{b}^e)^2 + J^e \frac{\partial U}{\partial J^e} \mathbf{I}. \quad (55)$$

For the special case of a neo-Hookean material with the Lamé constants λ and μ , such that $c_1 = \frac{1}{2}\mu$, $c_2 = 0$, $d_1 = \frac{1}{2}\lambda$, and $d_2 = -\mu$ (Kuhl, Menzel, & Steinmann, 2003), the free energy (53) reduces to

$$\psi = \frac{1}{2} \mu [I_1^e - 3] + \frac{1}{2} \lambda \ln^2(J^e) - \mu \ln(J^e), \quad (56)$$

and the neo-Hookean Kirchhoff stress (55) becomes

$$\boldsymbol{\tau} = 2 \frac{\partial \psi}{\partial \mathbf{b}^e} \cdot \mathbf{b}^e = \mu \mathbf{b}^e + [\lambda \ln(J^e) - \mu] \mathbf{I}. \quad (57)$$

It remains to specify the growth kinematics and growth kinetics for gray and white matter tissue.

The gray matter tissue of the cerebral cortex is mainly made up of neurons, which migrate to the surface of the brain along radial glial cells (Welker, 1990). While the cortical thickness changes during these early stages of neurodevelopment (Smart & McSherry, 1986), during the later stages, it is primarily the change in surface area that triggers cortical folding. It seems reasonable to assume that gray matter growth is an in-plane area growth and that the response normal to the cortical surface is purely elastic (Holland et al., 2015). The resulting gray matter growth tensor is transversely isotropic with a preferred direction \mathbf{n}_0 normal to the cortical surface (Zöllner, Holland, Honda, Gosain, & Kuhl, 2013),

$$\mathbf{F}^g = \sqrt{\vartheta^g} \mathbf{I} + [1 - \sqrt{\vartheta^g}] \mathbf{n}_0 \otimes \mathbf{n}_0. \quad (58)$$

The gray matter growth parameter ϑ^g represents the increase in cortical surface area,

$$\vartheta^g = \|J^g \mathbf{F}^{g-t} \cdot \mathbf{n}_0\| = \det(\mathbf{F}^g) = J^g, \quad (59)$$

which is identical to the growth in gray matter volume J^g . The multiplicative decomposition of the deformation gradient (51) translates into the

multiplicative decomposition of the total cortical area change ϑ into an elastic area change ϑ^e and area growth ϑ^g ,

$$\vartheta = \|J\mathbf{F}^{-t} \cdot \mathbf{n}_0\| = \vartheta^e \vartheta^g. \quad (60)$$

Using the Sherman–Morrison formula, we can invert the growth tensor,

$$\mathbf{F}^{g-1} = \frac{1}{\sqrt{\vartheta^g}} \mathbf{I} + \frac{\sqrt{\vartheta^g} - 1}{\sqrt{\vartheta^g}} \mathbf{n}_0 \otimes \mathbf{n}_0, \quad (61)$$

and calculate the gray matter elastic tensor,

$$\mathbf{F}^e = \frac{1}{\sqrt{\vartheta^g}} \mathbf{F} + \frac{\sqrt{\vartheta^g} - 1}{\sqrt{\vartheta^g}} \mathbf{n} \otimes \mathbf{n}_0, \quad (62)$$

where $\mathbf{n} = \mathbf{F} \cdot \mathbf{n}_0$ is the grown cortical normal. We thus obtain an explicit expression for the elastic left Cauchy Green deformation tensor \mathbf{b}^e as the growth-weighted total left Cauchy Green deformation tensor \mathbf{b} , corrected by the term $[1 - 1/\vartheta^g] \mathbf{n} \otimes \mathbf{n}$ that ensures nonthickness growth,

$$\mathbf{b}^e = \frac{1}{\vartheta^g} \mathbf{b} + \left[1 - \frac{1}{\vartheta^g}\right] \mathbf{n} \otimes \mathbf{n} \quad \text{with } \mathbf{b} = \mathbf{F} \cdot \mathbf{F}^t. \quad (63)$$

The elastic left Cauchy Green deformation tensor \mathbf{b}^e directly enters the definition of the neo-Hookean Kirchhoff stress in Eq. (57). The simplest kinetic model for cortical growth is a linear morphogenetic model,

$$\dot{\vartheta}^g = G^{\text{ctx}}, \quad (64)$$

where G^{ctx} is the rate of cortical expansion. On the cellular level, the tangential expansion is associated with the maturation of the neocortex caused by an increase of neurons in size, the formation of corticocortical connections, and the addition of intracortical glia cells (Sun & Hevner, 2014).

The white matter tissue underneath the cerebral cortex consists largely of myelinated axons. Axons are capable of growing in length when exposed to chronic overstretch (Bray, 1984). This suggests to model white matter growth as fiber growth and assume that the response normal to the fiber direction is purely elastic (Holland et al., 2015). The resulting white matter growth tensor is transversely isotropic with a preferred direction \mathbf{a}_0 along the axonal direction (Zöllner et al., 2012),

$$\mathbf{F}^g = \mathbf{I} + [\lambda^g - 1] \mathbf{a}_0 \otimes \mathbf{a}_0. \quad (65)$$

The white matter growth parameter λ^g represents the chronic increase in length along the axonal vector, $\mathbf{a}^g = \mathbf{F}^g \cdot \mathbf{a}_0$,

$$\lambda^g = \|\mathbf{a}^g\| = \sqrt{\mathbf{a}_0 \cdot \mathbf{F}^{g^t} \cdot \mathbf{F}^g \cdot \mathbf{a}_0} = \det(\mathbf{F}^g) = J^g, \quad (66)$$

which is identical to the increase in white matter volume J^g and thus directly correlated to the cumulative growth of all axons in the white matter tissue. The multiplicative decomposition of the deformation gradient (51) translates into the multiplicative decomposition of the total stretch along the axon λ into an elastic part λ^c and a growth part λ^g , similar to the one-dimensional case in Section 3.1,

$$\lambda = \|\mathbf{a}\| = \sqrt{\mathbf{a}_0 \cdot \mathbf{F}^t \cdot \mathbf{F} \cdot \mathbf{a}_0} = \lambda^c \lambda^g. \quad (67)$$

Again, we use the Sherman–Morrison formula and invert the growth tensor,

$$\mathbf{F}^{g^{-1}} = \mathbf{I} + \frac{1 - \lambda^g}{\lambda^g} \mathbf{a}_0 \otimes \mathbf{a}_0, \quad (68)$$

to calculate the white matter elastic tensor,

$$\mathbf{F}^e = \mathbf{F} + \frac{1 - \lambda^g}{\lambda^g} \mathbf{a} \otimes \mathbf{a}_0, \quad (69)$$

where $\mathbf{a} = \mathbf{F} \cdot \mathbf{a}_0$ is the current axonal vector. We obtain the explicit expression for the elastic left Cauchy Green deformation tensor \mathbf{b}^e as a rank-one update of the total left Cauchy Green deformation tensor \mathbf{b} ,

$$\mathbf{b}^e = \mathbf{b} + \frac{1 - \lambda^{g^2}}{\lambda^{g^2}} \mathbf{a} \otimes \mathbf{a} \quad \text{with} \quad \mathbf{b} = \mathbf{F} \cdot \mathbf{F}^t. \quad (70)$$

Again, the elastic left Cauchy Green deformation tensor \mathbf{b}^e directly enters the definition of the neo-Hookean Kirchhoff stress in Eq. (57). White matter growth is primarily a result of chronic axonal elongation upon prolonged overstretch (Bray, 1984). This suggests the following kinetic ansatz,

$$\dot{\lambda}^g = G^{\text{axn}} \langle \lambda^c - \lambda^{\text{crit}} \rangle, \quad (71)$$

a special version of Eqs. (40) and (41), with unlimited growth. Similar to the one-dimensional model of chronic axonal elongation in Section 3.1, growth is activated only if the elastic stretch $\lambda^c = \lambda/\lambda^g$ exceeds the homeostatic equilibrium value λ^{crit} . The growth rate G^{axn} scales the speed of growth, which we calibrated in Section 3.1.1 for neurites to $G^{\text{axn}} = 0.5/\text{min}$ and in Section 3.1.2 for axons to $G^{\text{axn}} = 0.08 \text{ per h}$ (Holland et al., 2015).

3.3.1 Example: Morphogenesis from Axon Elongation

The human brain displays a highly anisotropic arrangement of axon fiber bundles. Figure 18 illustrates the variation in axon orientation across our brain using diffusion spectrum imaging (Bardin, 2012). Specifically, we can identify three distinct axon orientation patterns, radially straight I-shaped, radially curved V-shaped, and radially curved U-shaped.

Figure 18 illustrates the simulated brain surface morphology for varying axon orientations, from left to right, and increasing growth ratios, from top to bottom (Holland et al., 2015). The axon orientation clearly impacts the folding pattern, the gyral wavelength, and the sulcal depth. Anisotropic orientations generate irregular surface morphologies with locally varying gyral wavelengths and pronounced sulcal depths. As the growth ratio increases, the gray matter layer grows faster relative to the white matter core.

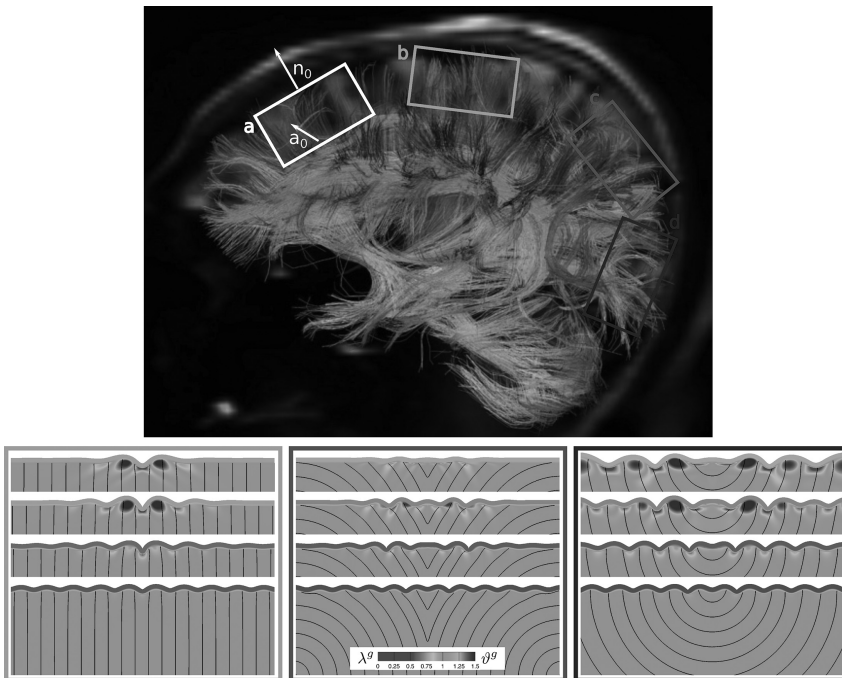


Figure 18 Varying axon orientations induce anisotropic growth. Diffusion spectrum imaging of the adult human brain reveals regionally varying cortical normals \mathbf{n}_0 and axonal orientations \mathbf{a}_0 (Bardin, 2012). Axons display radially straight I-shaped (left), radially curved V-shaped (middle), and radially curved U-shaped (right) orientations \mathbf{a}_0 . Color (different gray shades in the print version) contours indicate the computationally simulated axonal growth λ^g and cortical expansion θ^g (Holland et al., 2015).

The influence of white matter growth, and with it the degree of anisotropy, becomes less pronounced, and the surface morphology becomes more regular.

3.3.2 Example: Gyrogenesis in the Mammalian Brain

The mammalian brain varies impressively in size, shape, and convolucional complexity (Welker, 1990). Generally, the absolute brain size scales with body size (Welker, Johnson, & Noe, 2014). The brain surface area, however, increases disproportionately faster than the brain volume and larger brains appear more convoluted than smaller brains. This implies that the degree of gyrification varies significantly between species (Herculano-Houzel, 2009). Figure 19 illustrates the variation in size and gyrification in the squirrel, capybara, lion, and chimpanzee brains. The simulations of ellipsoids with a morphologically growing gray matter layer on a stretch-induced growing inner white matter core predict an increase in gyrification and cortical complexity with increasing radius-to-thickness ratio R/t (Budday, Steinmann, Goriely, & Kuhl, 2015). Figure 20 illustrates the

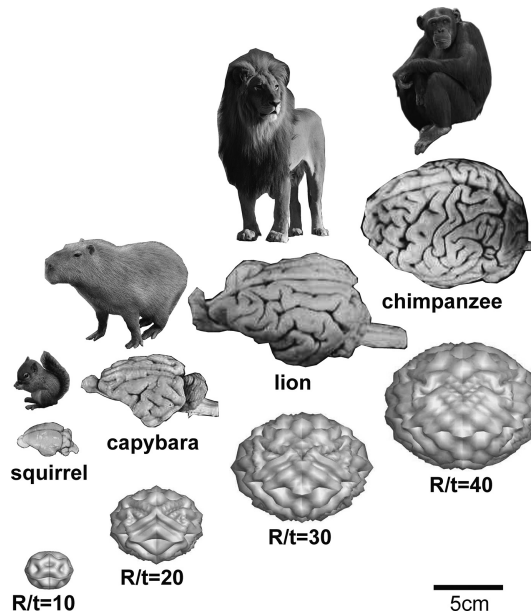


Figure 19 Mammalian brains vary greatly in size, shape, and gyrification but only marginally in cortical thickness (Welker et al., 2014). Simulations of a growing ellipsoid with varying radius-to-thickness ratio R/t predict an increase in gyrification and cortical complexity with increasing brain size (Budday, Steinmann, Goriely, & Kuhl, 2015).

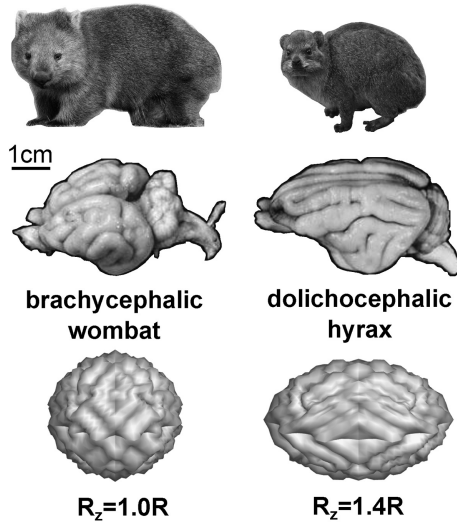


Figure 20 Mammalian brains vary greatly in ellipticity and gyrification (Welker et al., 2014). Simulations of a growing ellipsoid with varying ellipticity R_z/R predict transverse folding in the brachycephalic skull and longitudinal folding in the dolichocephalic skull (Budday, Steinmann, Goriely, & Kuhl, 2015).

variation in ellipticity and gyrification in the wombat and hyrax brains. The simulations predict pronounced transverse folding in the brachycephalic skull and longitudinal folding in the dolichocephalic skull with increasing ellipticity R_z/R (Budday, Steinmann, Goriely, & Kuhl, 2015). These findings agree with cortical folding in the mammalian brain, where transverse folding dominates in the brachycephalic Chinese skull, whereas longitudinal folding predominates in the dolichocephalic Dutch skull (van Bork-Feltkamp, 1930).

As pointed out more than half a century ago by Sir Wilfrid Le Gros Clark (Le Gros Clark, 1945), both genetic and mechanical factors affect cortical folding during brain development. To date, hypotheses on how convolutions in the mammalian brain evolve (Finlay & Darlington, 1995) and which forces drive the folding process (Richman et al., 1975; Van Essen, 1997) remain contradictory. A promising mechanical explanation of brain folding is based on differential growth, which gives rise to residual stresses that induce a mechanical instability, which results in surface buckling (Ciarletta et al., 2014). The stress patterns associated with differential growth theories in Figures 19 and 20 agree well with physical stress measurements in developing ferret brains (Smart & McSherry, 1986).

3.3.3 Example: Pathogenesis of Lissencephaly and Polymicrogyria

Malformations, as a result of interrupted cortical development, are a common cause of mental disorders including developmental delay and epilepsy (Barkovich, Guerrini, Kuzniecky, Jackson, & Dobyns, 2012). Brain function is closely correlated to brain structure and it is essential to understand how and why structural abnormalities form (Bayly et al., 2014). Mechanical modeling of brain development can explain malformations and variations of gyral wavelengths in healthy and diseased human brains (Richman et al., 1975). A misbalance in growth or cortical thickness can cause morphological abnormalities: A slower growing or thinner cortex generally enhances folding; a faster growing or thicker cortex reduces folding (Budday, Raybaud, & Kuhl, 2014). These characteristics can help explain the classical pathologies of lissencephaly and polymicrogyria (Raybaud & Widjaja, 2011).

Figure 21 illustrates the pathology of lissencephaly, a migration disorder associated with a smooth brain (Budday, Steinmann, & Kuhl, 2015a). During neuronal migration, a significant fraction of neurons fails to reach the outer cortex and remains underneath the cortical plate. Neuronal misplacement

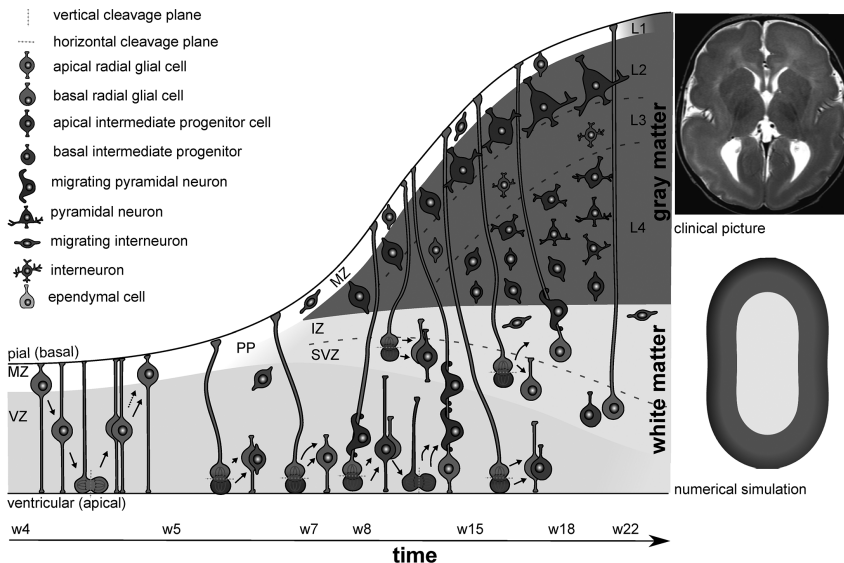


Figure 21 Lissencephaly is a migration disorder associated with a smooth brain. Cortical malformations result from abnormal neuronal migration during the early stages of neurogenesis. The extensively thickened cortex typically only consists of four disorganized layers. Consistent with the clinical picture of lissencephaly (top right), the numerical simulation (bottom right) predicts the absence of folds for extensively thickened cortices (Budday, Steinmann, & Kuhl, 2015a).

results in a severe defect of cortical connectivity and a markedly thickened cortex (Raybaud et al., 2013). Consistent with the pathology of lissencephaly (Budday, Raybaud, & Kuhl, 2014), the computational simulation of differential growth (Budday, Steinmann, & Kuhl, 2014) predicts that a considerably thickened cortex fails to fold. Its growth-induced compressive stresses are too small to induce buckling and the brain surface remains smooth.

Figure 22 illustrates the pathology of polymicrogyria, an organization disorder associated with many small folds (Budday, Steinmann, & Kuhl, 2015a). In comparison to the healthy six-layered human cortex, the polymicrogyric cortex consists of only four layers (Raybaud et al., 2013). This results in a reduced cortical thickness, and an increase in number and decrease in size of gyri and sulci. Consistent with the pathology of polymicrogyria (Budday, Raybaud, & Kuhl, 2014), the computational simulation of differential growth (Budday, Steinmann, & Kuhl, 2014) predicts

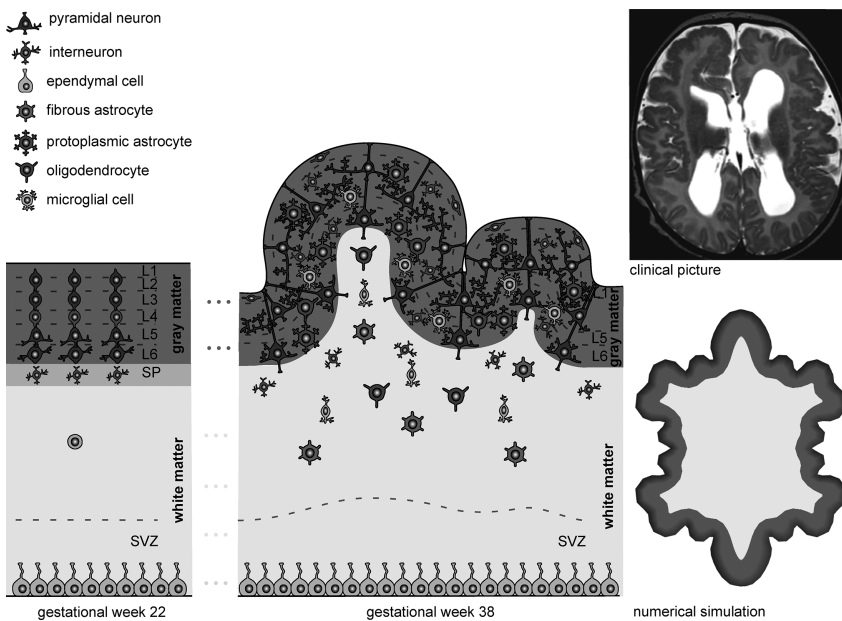
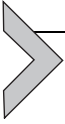


Figure 22 Polymicrogyria is an organization disorder associated with many small folds. Cortical malformations resulting from abnormal neuronal organization. Increased cellular necrosis and disturbed neuronal connectivity result in a thinned cortex with an excessive number of small irregular folds. Consistent with the clinical picture of polymicrogyria (top right), the numerical simulation (bottom right) predicts the emergence of many, small irregular folds for thin cortices and reduced growth of inner layers (Budday, Steinmann, & Kuhl, 2015a).

the emergence of small superficial folds as a result of cortical thinning and reduced growth in the subjacent layers. Understanding the mechanisms of cortical folding in the developing human brain can have direct implications on the diagnostics and treatment of neurological disorders, including severe retardation, epilepsy, schizophrenia, and autism.



4. NEURODAMAGE

Under large deformations, over short time scales, our brain becomes inelastic and vulnerable to damage. In this section, we focus on the inelasticity associated with neurodamage. We consider phenomena on relatively fast time scales, on which the brain is unable to respond to environmental changes. While rate effects may play a more significant role during damage than during elasticity and development, for the sake of clarity, here we focus primarily on rate-independent effects, but include rate-dependent effects when necessary. With these considerations in mind, we highlight the damage of single neurons in Section 4.1, the damage of gray and white matter tissue in Section 4.2, and the damage of the brain in Section 4.3. Similar to the previous sections, we complement the theory with experiments, illustrate what we can learn from these experiments, and discuss how these individual findings enrich our overall understanding of the brain as a whole.

4.1 Neurodamage of Single Neurons

At low stretch rates, axons can be stretched to multiples of their initial length without losing structural integrity (van den Bedem & Kuhl, 2015). At high stretch rates, however, e.g., during traumatic brain injury, axons experience microstructural damage and functional degradation (Tang-Schomer, Patel, Baas, & Smith, 2010). To model axonal damage, we can adapt the theory of continuum damage mechanics (Lemaître, 1992; Lemaître & Chaboche, 1985). To characterize the kinematics of axonal damage, we introduce the stretch λ as the ratio of unstretched axonal length L and stretched axonal length l ,

$$\lambda = l / L. \quad (72)$$

The basic idea of continuum damage mechanics is to represent the free energy function $\psi = [1 - d] W$ of the damaged material as the damage-weighted stored energy W of the undamaged, elastic material, e.g., of Mooney Rivlin type (2),

$$\psi = [1 - d] W \quad \text{with} \quad W = c_1 [I_1 - 3] + c_2 [I_2 - 3]. \quad (73)$$

The scalar-valued parameter d is the damage variable that takes the interpretation of the effective surface density of microdefects (Kachanov, 1958). It varies between $0 \leq d \leq 1$; it is zero for the intact axon and one for an entirely damaged axon. In analogy to Section 2, for the case of incompressibility and uniaxial tension, the stored energy W of the undamaged material reduces to the following expression,

$$\psi = [1 - d]W \quad \text{with} \quad W = c_1 \left[\lambda^2 + \frac{2}{\lambda} - 3 \right] + c_2 \left[2\lambda + \frac{1}{\lambda^2} - 3 \right]. \quad (74)$$

From Clausius Duhem inequality, we obtain the Piola stress P of the damaged material as the damage-weighted Piola stress \bar{P} of the elastic material,

$$P = \frac{d\psi}{d\lambda} = [1 - d] \bar{P} \quad \text{with} \quad \bar{P} = \frac{dW}{d\lambda} = 2 \left[c_1 + c_2 \frac{1}{\lambda} \right] \left[\lambda - \frac{1}{\lambda^2} \right]. \quad (75)$$

To characterize the damage kinetics, it is common to introduce a damage loading function,

$$\Phi = \phi(\lambda) - d(\kappa) \leq 0. \quad (76)$$

where κ is an internal variable that characterizes the history of damage. For diffuse axonal injury, we can assume that damage is strain driven, and that ϕ is a monotonic function of the stretch λ (Simo & Ju, 1987). From the dissipation inequality, we obtain the Kuhn–Tucker loading–unloading conditions,

$$\Phi \leq 0 \quad \dot{\kappa} \geq 0 \quad \dot{\kappa} \Phi = 0, \quad (77)$$

and the consistency condition, which introduces a closed-form update of the damage parameter d as a function of the damage history variable κ ,

$$\dot{\kappa} \Phi = 0 \quad \text{thus} \quad \dot{\lambda} = \dot{\kappa} \geq 0 \rightarrow d = \phi(\kappa). \quad (78)$$

The history variable κ records the maximum stretch $\lambda(s)$ during the loading history, $-\infty < s < t$, that exceeds an initial damage threshold κ_0 (Simo & Ju, 1987),

$$\kappa = \max_{-\infty < s < t} \{ \lambda(s), \kappa_0 \}. \quad (79)$$

In the initial damage theory, in accordance with second law of thermodynamics, damage can only increase, $\dot{d} \geq 0$. This implies that the axon is incapable of self-repair. A typical damage function could take the following format,

$$d = d_0 + [d_\infty - d_0] \exp(-\exp(\xi[\bar{\kappa} - \kappa])), \quad (80)$$

where d_0 is the initial damage, d_∞ is the maximum amount of damage, ξ controls the damage increase with increasing stretch, and $\bar{\kappa}$ is the damage threshold.

4.1.1 Example: Damaging Axons, Loss of Microtubules

In the classical interpretation of continuum damage mechanics (Kachanov, 1958), the damage parameter d represents the ratio between the damaged surface area and the total nominal surface area. As damage progresses, the effective load carrying area decreases. Figure 23 illustrates the reduction of the effective load carrying area in axons through the progressive loss of axonal microtubules (Tang-Schomer et al., 2010). Microtubules are long hollow cylinders made up of 13 protofilaments that surround the hollow center. With a diameter of 24 nm and an axial stiffness of the order of

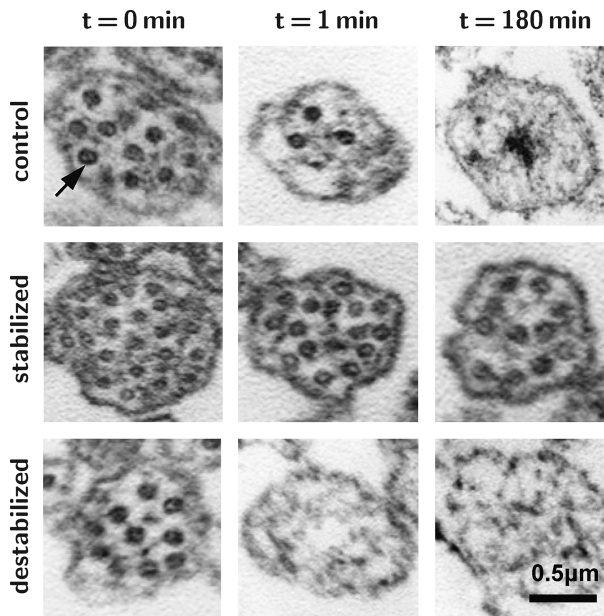


Figure 23 Axonal damage through progressive loss of microtubules. Initially, cross sections through the control axon, the taxon-stabilized axon, and the nocodazole-destabilized axon have similar numbers of microtubules shown as dark circular cross sections (arrow). When rapidly stretched beyond a critical stretch level, control axons gradually lose their microtubules. Stabilized axons maintain their microtubules; destabilized axons lose microtubules more rapidly (Tang-Schomer et al., 2010). Continuum damage models represent diffuse axonal injury as the relative loss in cross section area.

$EA \approx 10$ nN, microtubules constitute the major load bearing element of the axon (Alberts et al., 2014). A functional axon contains on average ten microtubules per cross section. The transmission electron microscope images in the left column show the initial cross sections of a representative control axon, a taxon-stabilized axon, and a nocodazole-destabilized axon, which have similar numbers of microtubules in the unloaded reference state. The axons were plated on a flexible substrate and subjected to controlled stretch. Under low stretch rates of the order of minutes, axons easily tolerated stretches up to twice their original length with no evidence of damage; under higher stretch rates of 44/s, axons display a progressive loss of microtubules (Tang-Schomer et al., 2010). The middle and left cross sections illustrate the three representative axons immediately after stretching and 3 h after stretching: 1 min after stretching, 33% of the control axons had lost all their microtubules, $d = 1$, compared to 1% of the taxol-stabilized axons and 47% of the nocodazole-destabilized axons. Three hours after stretching, 42% of the control axons were entirely damaged, compared to 10% of the taxol-stabilized and 70% of the nocodazole-destabilized axons. For a constant stretch rate, damage increased with varying total stretches of 30%, 50%, and 75% (Tang-Schomer et al., 2010). This study suggests that progressive loss of microtubules in response to rapid axonal elongation can be modeled as gradual loss in effective load carrying area using the theory of continuum damage mechanics (Lemaître & Chaboche, 1985). The damage parameter d would then represent the fractional loss of microtubules across the axon, varying from $d = 0$ for intact axons to $d = 1$ for axons that have lost all their microtubules.

4.2 Neurodamage of Gray and White Matter Tissue

When subjected to large deformations, brain tissue experiences a characteristic behavior, similar to filled elastomers, with a stress–strain curve that depends on the maximum loading previously experienced (Franceschini et al., 2006). This phenomenon is associated with irreversible softening and, for rubber-like materials, known as the Mullins effect (Mullins, 1969). The Mullins effect is associated with finite deformations, characterized through the deformation gradient,

$$\mathbf{F} = \nabla_X \boldsymbol{\varphi} . \quad (81)$$

Similar to the one-dimensional case, it can be represented through the free energy function $\psi = [1 - d]W$ of the damaged material as the damage-

weighted stored energy W of the undamaged, elastic material. For the stored energy W , we can, e.g., adopt an Ogden type model (19),

$$\psi = [1 - d]W \quad \text{with} \quad W = \sum_{p=0}^{\infty} \frac{1}{2^p} \frac{c_p}{m_p} \left[\lambda_1^{2m_p} + \lambda_2^{2m_p} + \lambda_3^{2m_p} - 3 \right], \quad (82)$$

or a Mooney Rivlin type model (20),

$$\psi = [1 - d]W \quad \text{with} \quad W = c_1 [I_1 - 3] + c_2 [I_2 - 3]. \quad (83)$$

Similar to the one-dimensional case, the scalar-valued parameter d is the damage variable that characterizes the effect of stiffness degradation (Kachanov, 1958). It varies between $0 \leq d \leq 1$, is zero for the initially intact material, and one for complete stiffness degradation. From the Clausius Duhem inequality, we obtain the three-dimensional Piola stress \mathbf{P} as the damage-weighted Piola stress $\bar{\mathbf{P}}$ of the elastic material (22),

$$\mathbf{P} = \frac{\partial \psi}{\partial \mathbf{F}} = [1 - d] \bar{\mathbf{P}} \quad \text{with} \quad \bar{\mathbf{P}} = \frac{\partial \bar{\psi}}{\partial \mathbf{F}} = 2[c_1 + c_2 I_1] \mathbf{F} - 2c_2 \mathbf{F} \cdot \mathbf{F}^t \cdot \mathbf{F} + J \frac{\partial U}{\partial J} \mathbf{F}^{-t}. \quad (84)$$

Similar to the elastic case in Section 2, the Kirchhoff stress $\boldsymbol{\tau} = \mathbf{P} \cdot \mathbf{F}^t$ simply follows from its push forward,

$$\boldsymbol{\tau} = 2 \frac{\partial \psi}{\partial \mathbf{b}} \cdot \mathbf{b} = [1 - d] \bar{\boldsymbol{\tau}} \quad \text{with} \quad \bar{\boldsymbol{\tau}} = \frac{\partial \bar{\psi}}{\partial \mathbf{b}} = 2[c_1 + c_2 I_1] \mathbf{b} - 2c_2 \mathbf{b}^2 + J \frac{\partial U}{\partial J} \mathbf{I}. \quad (85)$$

To characterize the state of loading, we introduce a damage loading function,

$$\Phi = \phi(W) - d(\kappa) \leq 0, \quad (86)$$

where κ is an internal variable that characterizes the damage history and ϕ is a monotonic function of the strain \mathbf{E} or, in the case of thermodynamic consistency, of the elastic stored energy W (Franceschini et al., 2006). From the dissipation inequality, we obtain the Kuhn–Tucker loading–unloading conditions,

$$\Phi \leq 0 \quad \dot{\kappa} \geq 0 \quad \dot{\kappa} \Phi = 0, \quad (87)$$

and the consistency condition, which allows for a closed-form update of the damage parameter d in terms of the damage history variable κ ,

$$\dot{\kappa} \dot{\Phi} = 0 \quad \text{thus} \quad \dot{\lambda} = \dot{\kappa} \geq 0 \rightarrow d = \phi(\kappa). \quad (88)$$

The history variable κ records the maximum elastic stored energy W above an initial damage threshold κ_0 during the loading history, $-\infty < s < t$,

$$\kappa = \max_{-\infty < s < t} \{W(s), \kappa_0\}. \quad (89)$$

For the damage function, we could simply use the same damage function as for the one-dimensional case (80),

$$d = d_0 + [d_\infty - d_0] \exp(-\exp(\xi[\bar{\kappa} - \kappa])), \quad (90)$$

where d_0 is the initial damage, d_∞ is the maximum amount of damage, ξ controls the damage increase with increasing stretch, and $\bar{\kappa}$ is the damage threshold. Alternatively, we could adapt a function proposed initially to model the Mullins effect in rubber-like materials (Ogden & Roxburgh, 1999),

$$d = \text{erf}((\bar{W} - W)/m)/r \quad (91)$$

where $\text{erf}(x) = 2/\sqrt{\pi} \int_0^x \exp(-t^2) dt$ is the error function, r and m are material parameters, and \bar{W} represents the stored energy associated with the maximum principal stretch $\bar{\lambda}$ obtained in the loading history (Franceschini et al., 2006). For both damage functions (90) and (91), the evolution of damage is purely driven by the stretch itself. To model the effect of axonal damage at high strain rates (Pfister et al., 2004), we can parameterize the damage function in terms of the strain and strain rate (Lemaître, 1992). Recent studies in an *in vitro* traumatic brain injury model with varying strains and strain rates found, however, that cell death was sensitive to the strain, but rather insensitive to the strain rate (Cater, Sundstrom, & Morrison III, 2006).

4.2.1 Example: Damage of the Hippocampal Tissue, Cell Death

Brain tissue damage involves complex mechanotransduction pathways that are virtually impossible to attribute to a single mechanical variable alone. Even below ultimate failure limits, mechanical strain can activate pathophysiological cascades, which result in cell death that gradually accumulates in time. In an *in vitro* model of traumatic brain injury based on equibiaxially stretched hippocampal slice cultures, a recent study quantified brain tissue damage as the percent area of propidium iodide staining, a marker for cell death, in the CA1 and CA3 regions and in the dentate gyrus (Cater et al., 2006).

Figure 24 illustrates the increase in hippocampal tissue damage with increasing strain. The white circles represent the experimentally characterized cell death in the CA1 and CA3 regions of the hippocampus at different strain levels 3 and 4 days after injury. The white circles and squares represent the cell death in the CA1 and CA3 regions and in the dentate gyrus at different strain levels 4 days after injury (Cater et al., 2006). We can use these data to calibrate a damage function similar to Eq. (80),

$$d = d_0 + [d_\infty - d_0] [1 - \exp(-\xi[\kappa - \bar{\kappa}])]$$

where the history variable κ records the maximum Green Lagrange strain E during the loading history, $-\infty < s < t$,

$$\kappa = \max_{-\infty < s < t} \{E(s), \kappa_0\},$$

and $d_0 = 0$ is the initial damage, d_∞ is the maximum amount of damage, ξ controls the damage slope, and $\kappa_0 = 0$ and $\bar{\kappa} = 0$ are the damage thresholds. The color coded regions illustrate the effects of varying the damage slope ξ and the maximum damage d_∞ . The thick lines display the best fits for $\xi = 2.5$ and $\xi = 7.5$ at days three and four and for $d_\infty = 0.30$ and $d_\infty = 0.48$ in the CA1 and CA3 regions and in the dentate gyrus. These graphs suggest that brain tissue damage is a temporally and spatially varying process that is

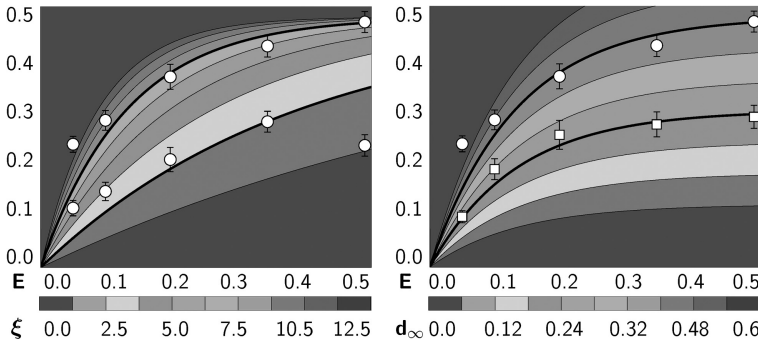


Figure 24 Hippocampal tissue damage increases with increasing strain. White circles represent experimentally characterized cell death in the CA1 and CA3 regions of the hippocampus at different strain levels 3 and 4 days after injury (left) (Cater et al., 2006). White circles and squares represent cell death in the CA1 and CA3 regions and in the dentate gyrus at different strain levels 4 days after injury (right) (Cater et al., 2006). Color (different gray shades in the print version) coded regions illustrate the effects of varying the damage slope ξ and the maximum damage d_∞ . Thick lines display the best fits for $\xi = 2.5$ and $\xi = 7.5$ at days 3 and 4 (left) and for $d_\infty = 0.30$ and $d_\infty = 0.48$ in the CA1 and CA3 regions and in the dentate gyrus (right).

driven, at least in part, by the applied strain and the postinjury time: Damage increases gradually with postinjury time, suggesting that the scaling exponent ξ is not a constant but a time-dependent parameter. Different regions display a different vulnerability to strain, suggesting that the maximum damage d_∞ is regionally dependent. In addition to these findings, this study also found that cell death was rather insensitive to the strain rate (Cater et al., 2006).

4.2.2 Example: Damage of Nervous Tissue, Area Degradation

Diffuse axonal injury is the most frequent type of closed head injury and the second largest cause of death due to brain trauma. It manifests itself through axonal damage in the white matter tissue; however, little is known about the tissue level damage thresholds for axonal injury. A recent study characterized the damage thresholds for the model system of the optical nerve of an adult male guineapig (Bain, Raghupathi, & Meaney, 2001) using neurofilament immunohistochemical staining.

Figure 25 shows two representative neurofilament immunostains with NF68, a marker to visualize nervous tissue damage. The study identified three strain-based thresholds $\bar{\kappa}$ for morphological damage to white matter tissue in terms of the Green Lagrange strain $E = \frac{1}{2} [\lambda^2 - 1]$: the conservative threshold at $\bar{\kappa} = 0.14$, the level below which no axons display injury, $d = 0$; the liberal threshold at $\bar{\kappa} = 0.34$, the level above which all axons display injury, $d = 1$; and the optimal threshold at $\bar{\kappa} = 0.21$.

Figure 26 illustrates the increase in nervous tissue damage with increasing strain. The white circles represent the experimentally characterized damaged, $d = 1$, and undamaged, $d = 0$, tissue samples at different strain levels. The black circles indicate the conservative damage threshold at 14% strain,

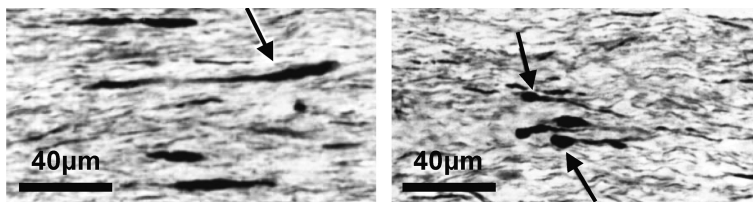


Figure 25 Nervous tissue damage visualized through neurofilament immunostaining with NF68, a marker for axonal pathology (Bain & Meaney, 2000). Damaged tissue displays clusters of retraction bulbs (left arrow) and axonal swelling (right arrows). Continuum damage models represent damage as the relative loss in cross section area.

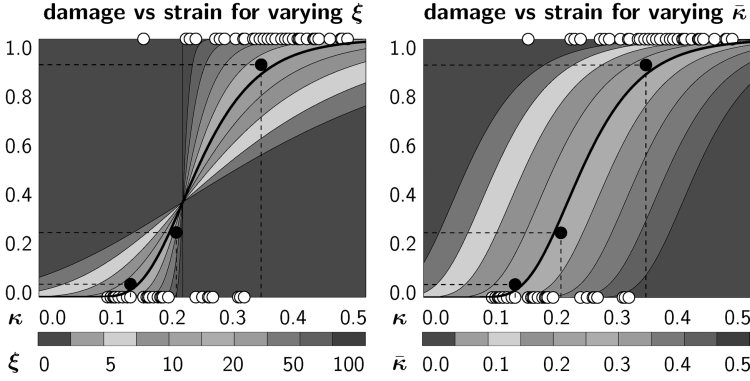


Figure 26 Nervous tissue damage increases with increasing strain. White circles represent experimentally characterized damaged, $d = 1$, and undamaged, $d = 0$, tissue samples at different strain levels (Bain & Meaney, 2000). Black circles define conservative damage threshold at 14% strain, liberal damage threshold at 34% strain, and optimal damage threshold at 21% strain (Bain & Meaney, 2000). Color (different gray shades in the print version) coded regions illustrate the effects of varying the damage slope ξ and the optimal damage threshold $\bar{\kappa}$. Thick lines display the best fit for $\xi = 16$ and $\bar{\kappa} = 21\%$.

the liberal damage threshold at 34% strain, and the optimal damage threshold at 21% strain (Bain & Meaney, 2000). We can use these data to calibrate the damage function in Eq. (90), with $d_0 = 0$ and $d_\infty = 1$,

$$d = \exp(-\exp(-\xi[\kappa - \bar{\kappa}])),$$

where the history variable κ records the maximum Green Lagrange strain $E = \frac{1}{2}[\lambda^2 - 1]$ during the loading history, $-\infty < s < t$,

$$\kappa = \max_{-\infty < s < t} \{E(s), \kappa_0\},$$

ξ controls the damage slope, and $\kappa_0 = 0$ and $\bar{\kappa}$ are the damage thresholds. The color coded regions illustrate the effects of varying the damage slope ξ and the optimal damage threshold $\bar{\kappa}$. The thick black lines display the best fit for $\xi = 16$ and $\bar{\kappa} = 0.21$. This suggests that nervous tissue damage is a gradual process that is driven, at least in part, by the applied strain (Lemaître & Chaboche, 1985). Although this particular study was calibrated for guinea pig optical nerve, and evidence suggests that brain tissue does not vary significantly between different species, it remains to be shown that similar thresholds are valid for human axonal injury (Bain & Meaney, 2000).

4.2.3 Example: Damage of Brain Tissue, Mullins Effect

To characterize the behavior of human brain tissue, a recent study performed a systematic series of *in vitro* experiments of human tissue samples excised during autopsy within 12 h of death (Franceschini et al., 2006). Under cyclic loading at strain rates on the order of 0.01 per s, up to a stretch level far from failure but near damage initiation, all white matter samples displayed strong nonlinearity, hysteresis, and different stiffnesses during tension and compression and during loading and unloading. The latter phenomenon is a clear evidence of the Mullins effect (Mullins, 1969) associated with damage-induced stiffness degradation.

Figure 27 illustrates the stress–stretch response under successive compression tension loading for two representative samples of white matter tissue, one from the frontal lobe in the sagittal direction and one from the occipital lobe in the frontal direction. The white circles summarize the experimental measurements. The solid lines display the simulation with the Ogden Roxbaugh model (Ogden & Roxburgh, 1999) with a free energy,

$$\psi = [1 - d]W,$$

where d is the damage parameter to account for the Mullins effect (91),

$$d = \operatorname{erf}((\bar{W} - W)/m)/r, \quad (92)$$

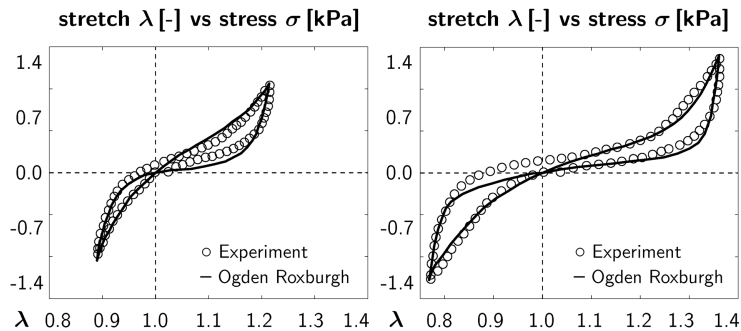


Figure 27 White matter damage and Mullins effect in compression tension experiments. White circles represent the stress–stretch response of white matter specimen from the frontal lobe in the sagittal direction (left) and from the occipital lobe in the frontal direction (Franceschini et al., 2006). Solid lines display the simulation with the Ogden Roxbaugh model (Ogden & Roxburgh, 1999).

and W is the stored energy of the two-parameter Ogden model (82) for the special case of incompressibility, $\lambda_1 \lambda_2 \lambda_3 = 1$, and uniaxial tension, $\lambda_1 = \lambda$ and $\lambda_2 = \lambda_3 = 1/\lambda^{1/2}$,

$$W = \frac{1}{2m_1} c_1 [\lambda^{2m_1} + 2\lambda^{-m_1} - 3] + \frac{1}{2m_2} c_2 [\lambda^{2m_2} + 2\lambda^{-m_2} - 3].$$

For the frontal lobe, the Ogden Roxbaugh parameters are $m_1 = -5.4$, $m_2 = 9.8$, $c_1 = -0.29$ kPa, $c_2 = 0.0096$ kPa, $r = 1.2$, and $m = 0.05$, with maximum compressive and tensile stretches of $\bar{\lambda}^- = 0.89$ and $\bar{\lambda}^+ = 1.21$; for the occipital lobe, they are $m_1 = 11.8$, $m_2 = -2.0$, $c_1 = 0.0008$ kPa, $c_2 = -0.41$ kPa, $r = 1.6$, and $m = 0.035$, with maximum compressive and tensile stretches of $\bar{\lambda}^- = 0.77$ and $\bar{\lambda}^+ = 1.36$ (Franceschini et al., 2006). This study suggests that mechanical loading beyond a physiological threshold level not only induces brain tissue damage, but that this damage is associated with marked stiffness degradation. This stiffness degradation could explain the increased vulnerability to repeated mild traumatic brain injury (Prins, Alexander, Giza, & Hovda, 2013).

4.3 Neurodamage of the Brain

Finite element analysis has become a popular tool to quantify regional effects of neurodamage and identify mechanisms of traumatic brain injury. Throughout the past decade, finite element head models of varying complexity have been developed, calibrated, and thoroughly refined (Songbai et al., 2014). Initially designed to assess the injury risk in car crashes (Takhounts, Eppinger, Campbell, & Tannous, 2003), these models now gain increasing popularity in sport-related injuries, where at-risk athletes can directly be equipped with instrumented helmets or mouthguards (Camarillo, Shull, Mattson, Shultz, & Garza, 2013).

Figure 28 illustrates a widely used finite element model of the human head (Kleiven & von Holst, 2002). The model was created from the visible human database and consists of the three layers of the skull, facial bones, scalp, cerebrum, cerebellum, spinal cord, dura mater, tentorium, and falx. The discretization uses a total of 16,909 nodes, 22 two-noded truss elements, 10,165 four-nodes shell and membrane elements, and 11,158 eight-noded brick elements, of which 7128 make up the brain (Kleiven, 2007). The model was validated against relative head motion experiments (Kleiven & von Holst, 2002) and intra-cerebral acceleration experiments (Kleiven, 2006).

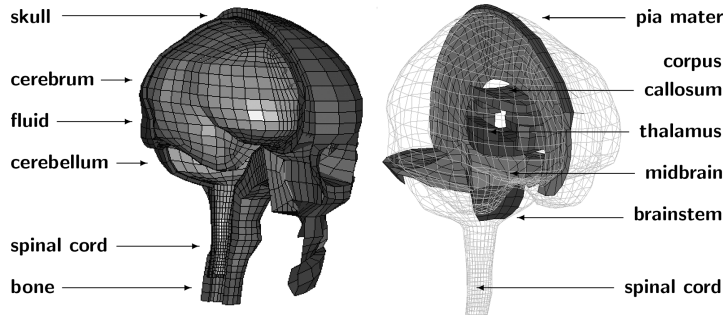


Figure 28 Finite element model of the human head created from the visible human database (Kleiven & von Holst, 2002). The model consists of the three layers of the skull, facial bones, scalp, cerebrum, cerebellum, spinal cord, dura mater, tentorium, and flax discretized with 16,909 nodes, 22 two-noded truss elements, 10,165 four-nodes shell and membrane elements, and 11,158 eight-noded brick elements, of which 7128 make up the brain (Kleiven, 2007).

To date, finite element head models are typically not used in the spirit of continuum damage mechanics along the lines of Section 4.2. Rather, they are used to identify critical tissue level damage thresholds that translate into local loss of brain function. We illustrate such an example in the following section.

4.3.1 Example: Damage Criteria, Strain and Strain Rate

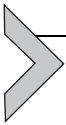
The current gold standard to assess damage to the head is the Head Injury Criterion (National Highway Traffic Safety Administration, 1972). Proposed more than four decades ago, this criterion attributes brain damage exclusively to translational acceleration and entirely ignores the rotational effects (Goriely et al., 2015). To compare the relevance of translational and rotational loading, a recent study utilized acceleration measurements of 58 cases from the National Football League to predict neuronal stresses and strains using the finite element model of Figure 28. The study modeled brain tissue with a two-parameter Ogden model (82),

$$W = \frac{1}{2} \frac{c_1}{m_1} [\lambda^{2m_1} + 2\lambda^{-m_1} - 3] + \frac{1}{2} \frac{c_2}{m_2} [\lambda^{2m_2} + 2\lambda^{-m_2} - 3] + \frac{1}{2} \kappa [J - 1]^2,$$

supplemented by a volumetric term, $\kappa [J - 1]^2 / 2$, where κ is the bulk modulus. The Ogden parameters were calibrated to $m_1 = 5.1$, $m_2 = -6.5$, $c_1 = 53.8$ Pa, and $c_2 = -120.4$ Pa (Kleiven, 2007), using the cyclic tissue-level compression-tension experiments (Franceschini et al., 2006) from the study

highlighted in Section 4.2. To account for rate effects, a convolution-integral-type viscous stress based on a six-term Prony series was added to the constitutive model (Kleiven, 2007).

For nine individual mechanical metrics including gray and white matter strain, strain rate, stress, and pressure, the study predicted the injury probability and systematically compared it against the probability of concussion. The comparison revealed that rotational kinematics significantly affect intracranial deformations, while translational kinematics affect the intracranial pressure (Kleiven, 2007). The study further reports that strain-based injury predictors are highly sensitive to the stiffness of both gray and white matter tissue. Recent follow up studies also highlight the importance of white matter anisotropy and the sensitivity with respect to local axon orientations (Cloots et al., 2011). Probably the most advanced finite element brain model to date is a multiscale model that uses the finite element model from Fig. 28, with a microlevel critical volume element attached to each integration point of interest (Cloots, van Dommelen, Kleiven, & Geers, 2013). This model suggests that tissue level strains do not consistently scale with the maximum axonal strain and concludes that a local resolution of the microstructure is critical to appropriately link the individual scales.



5. OPEN QUESTIONS AND CHALLENGES

While many scientists believe that understanding the human brain is primarily a question of biochemical and electrical events, increasing evidence suggests that mechanical regulators play an equally important role in neuronal development, degeneration, regeneration, and aging (Franze et al., 2013). In this review, we have highlighted selected pathologies which undoubtably show a mechanical trace, including the prominent examples of axon elongation (Suter & Miller, 2011), cortical folding (Xu et al., 2010), axon degeneration (Tang-Schomer et al., 2010), and traumatic brain injury (Meaney, Morrison, & Bass, 2014). While we are beginning to recognize the impact of mechanics on neurological events, there is no general theoretical framework that ties the individual pieces of information together (Goriely et al., 2015). The nonlinear field theories of mechanics provide a natural common platform to characterize the human brain within a holistic multi-scale, coupled fields approach. This strategy has proven successful for many other organs including bones, arteries, muscle, and skin, and there is no reason why a concerted effort along the same principles should not work equally well for the brain.

A first step towards a multiscale continuum model for the brain is to establish mechanistic constitutive models with physically meaningful parameters and calibrate these models for a wide range of loading conditions across scales, space, and time (Prevost, Balakrishnan, Suresh, & Socrate, 2011). In the past, experiments to characterize neuronal tissue have investigated the constitutive response under compression (Miller & Chinzei, 1997), shear (Bilston et al., 2001), and sometimes tensile loading (Miller & Chinzei, 2002), but hardly ever under cyclic compression-tension loading (Franceschini et al., 2006) or under combined loading conditions (Pogoda et al., 2014). Not surprisingly, the reported stiffness values vary by orders of magnitude, not only because of different experimental conditions (Hrapko, van Dommelen, Peters, & Wismans, 2008), but mainly because of different types of loading (Chatelin et al., 2010). More complex experiments are needed to truly understand the constitutive behavior of the brain under physiological loading conditions.

There is a growing agreement that appropriate constitutive models for neuronal tissue should at least capture the highly nonlinear, strain-stiffening response, the different response in tension, compression, and shear, and the Mullins effect of history dependence (Franceschini et al., 2006). These features are inherent to most rubber-like materials, which are commonly characterized by the classical Ogden model (Ogden, 1972) and its Mullins effect-type variants (Ogden & Roxburgh, 1999). Consequently, there is a growing trend to adopt Ogden-type models to characterize neuronal tissue (Bilston et al., 2001; Hrapko et al., 2006). In fact, the Mooney Rivlin model, a special subclass of the Ogden family with only two material parameters, seems outperform more complex constitutive models under specific conditions (Rashid et al., 2013). The successful use of these models demonstrates that a continuum approach is valid for the brain (Mihai et al., 2015). However, a major and well-known deficiency of Ogden-type modeling becomes immediately apparent from the examples highlighted in this review (Ogden, 1984): The Ogden parameters are purely phenomenological, they have no real physical interpretation, and they not only vary by several orders of magnitude, but also by sign. Ogden models are at a high risk of overfitting; they not only fit the physical behavior, but also possible measurement errors. It is only by understanding the microscopic origin of elasticity, growth, and damage, that we will be able to successfully model extremely soft matter on the continuum scale.

The inherent drawbacks of phenomenological models open tremendous opportunities for multiscale modeling, from individual neurons, via

neuronal tissue, to the brain as a whole (Cloots et al., 2013). In this review, we have made a first step towards a unified characterization of neuromechanics across the scales using the nonlinear field theories of mechanics. The handshake between the scales raises at least two major questions that point towards critical next steps: How does our knowledge from single cell experiments translate into tissue level properties, and how does *ex vivo* testing of isolated tissue samples translate into the behavior of the living brain? To answer the first question, it will be critical to identify the key mechanical players in neuronal tissue (Budday, Steinmann, & Kuhl, 2015a). What are the roles of neuronal connections, glial cells, and extracellular matrix, and how do all these components interact (Franze, 2013)? To address the second question, it will become important to understand the role of anisotropy, structural heterogeneity, and the difference between gray and white matter tissue (Cloots et al., 2011). What are the roles of the cerebrospinal fluid, the ventricles, the vasculature, and the skull (Abbot, 2004)? Including these additional effects will naturally lend itself towards a systems-based approach (Buganza & Kuhl, 2013), which will inherently introduce internal length scales via the diffusion equations that govern the additional fields (Garikipati, Arruda, Grosh, Narayanan, & Calve, 2004). Eventually, answering these questions will help us to understand how mechanical fields interact with biological, chemical, electrical, and thermal fields and vice versa (Lang, Stewart, Vella, Waters, & Goriely, 2014).

Multiscale modeling is a powerful technique that combines mathematical models and computational tools to fundamentally understand the human brain (Cloots et al., 2013). To link information from the molecular, cellular, tissue, and organ levels, multiscale models need to pass physical and structural knowledge across multiple length and time scales (De, Hwang, & Kuhl, 2015). This not only adds conceptual complexity, but also numerous additional parameters and possible constitutive relationships between them (Holland et al., 2015). Yet, the available *in vivo* information is often sparse, live measurements are difficult to obtain, and the characteristic features are specific to each patient. For calibration and validation, multiscale models of the brain can draw on a variety of sources including histological, anatomical, structural, physical, and clinical data. Machine learning across the scales provides a promising strategy to extract knowledge from these diverse data sets and infer physical laws and models, as well as their parameters, from clinical and experimental measurements (Macyszyn et al., 2015; Memarian, Kim, Dewar, Engel, & J., 2015). Multiscale neuromechanics modeling—possibly combined with machine learning—is now increasingly recognized as a

possible path towards integrating diverse data, creating testable hypotheses, identifying knowledge gaps, uncovering biological mechanisms, and making reliable predictions about clinical outcomes and neurosurgical interventions.

Ultimately, the driving force of neuromechanics is to understand how this integrated knowledge translates into brain function. For the example of elasticity, alterations in stiffness have been associated with aging and neurodegenerative disorders (Sack et al., 2009). Multiple sclerosis, a degenerative disease that affects neuronal myelination, manifests itself in a reduced *in vivo* stiffness, which is eventually related to reduced function (Streitberger et al., 2012). In this case, neuromechanics can help rationalize new diagnostic tools to classify disease progression. For the example of growth and development, alterations in cortical thickness and gray and white matter stiffness have a direct impact on cortical folding and gyral wavelengths (Bayly et al., 2013). Lissencephaly and polymicrogyria, cortical malformations with significantly increased and reduced gyral wavelengths, are associated with seizures, motor dysfunction, and severe retardation (Raybaud et al., 2013). Similar malformations, but regionally limited, are common to schizophrenia (Wisco et al., 2007) and autism spectrum disorders (Hardan, Jou, Keshavan, Varma, & Minshew, 2004). In these cases, neuromechanics can help identify early markers of disease to accelerate and improve treatment options. For the example of damage, alterations in axonal and white matter integrity directly impact electrical signal propagation (Jérusalem, García-Grajales, Merchán-Perez, & Peña, 2014). Traumatic brain injury, brain damage induced by rapid mechanical accelerations or decelerations, manifests itself in a wide variety of symptoms related to the functions of the damage area (Meaney et al., 2014). In this case, neuromechanics can help quantify the amount of brain damage that cannot be diagnosed with conventional imaging tools (Cloots et al., 2013).

The objective of this review was to bring these individual disciplines closer together and stimulate discussion and future research in the field of neuromechanics. We believe that neuromechanics has the potential to provide an essential missing link to connect brain structure, function, and ultimately behavior.

ACKNOWLEDGMENTS

This study was supported by the Wolfson/Royal Society Merit Award and the EC Reintegration Grant under Framework VII to A.G., the German National Science Foundation grant STE 544/50-1 to S.B.; and the National Science Foundation INSPIRE grant 1233054 and the National Institutes of Health Grant U54GM072970 to E.K.

GLOSSARY

- Axon** Long, slender projection from the cell body of a nerve cell, or neuron, that transmits electrical signals from the cell body to other neurons.
- Cerebral Cortex** Outer 2–4 mm-thick gray matter layer around the brain that consists primarily of cell bodies and plays an important role in attention, awareness, unconsciousness, language, memory, and thought.
- Cerebrospinal Fluid** Clear and colorless body fluid that acts as a cushion for the cerebral cortex and provides a basic mechanical protection for the brain inside the skull.
- Dendrite** Short, branched projection from the cell body of a nerve cell, or neuron, that propagates electrical signals from other neurons to the cell body.
- Diffuse Axonal Injury** Brain injury in the form of extensive lesions in the white matter tissue; one of the most common and devastating types of traumatic brain injury, and a major cause of unconsciousness and persistent vegetative state after head trauma.
- Glial Cell** Nonneuronal cell in the brain that maintains homeostasis, forms myelin, and provides structural support and protection for neurons.
- Gray Matter** Outer layer of the brain consisting mainly of neuronal cell bodies, glial cells, dendrites, and myelinated and unmyelinated axons; primarily associated with information processing and cognition; has a characteristic darker color because of it contains numerous cell bodies and relatively few myelinated axons.
- Gyrus** Ridge on the cerebral cortex surrounded by one or more sulci; gyri and sulci create the characteristic folded appearance of the brain in humans and other mammals.
- Gyrification** Process of folding of the cerebral cortex that permits a larger cortical surface area within the limited space of the skull; in mammalian brains, gyrification begins during embryogenesis; rodent brains do not undergo gyrification and remain flat.
- Head Injury Criterion** Measure of the likelihood of head injury caused by impact; used to assess safety related to vehicles, personal protective gear, and sport equipment.
- Homeostasis** Process of dynamic self-regulation that allows a living system to compensate for environmental changes and maintain a dynamic equilibrium state.
- Lissencephaly** Developmental malformation caused by a migration disorder associated with a thick cerebral cortex and a smooth brain surface.
- Meninges** Membranes that envelop the brain to provide protection; consist of three layers, the dura mater, arachnoid mater, the pia mater.
- Microtubules** Long, hollow cylindrical filaments made up of tubulin dimers; major load-bearing element of the axon; responsible for axonal organization, structure, and transport; functional axons contain on average ten microtubules per cross section.
- Morphogenesis** Biological process that causes an organism to develop its shape; controls the organized spatial distribution of cells during the embryonic development.
- Multiple Sclerosis** Nervous system disease associated with the demyelination of axons resulting in disrupted neuronal communication; associated with changes in mechanical properties including white matter stiffness.
- Myelination** Production of the myelin sheath, the fatty, electrically insulating layer around the axon to ensure proper signal conduction; associated with changes in mechanical properties including white matter stiffness.
- Neurite** Projection from the cell body of a nerve cell, or neuron; the term neurite refers to either an axon or a dendrite and is used for immature or developing neurons in culture before differentiation is complete.

- Neuron** Electrically excitable cell that transmit information through the brain via electrical and chemical signals; a typical neuron consists of a cell body, an axon, and multiple dendrites.
- Polymicrogyria** Developmental malformation caused by an organization disorder associated with a thin cerebral cortex and many small folds.
- Sulcus** Depression or groove in the cerebral cortex surrounding a gyrus; gyri and sulci create the characteristic folded appearance of the brain in humans and other mammals.
- Tau Protein** Cross-linking protein that stabilizes the microtubules in the axon; plays a critical role in in Alzheimer's disease and Parkinson's disease, where defective tau proteins can no longer stabilize microtubules properly; diseases are associated with changes in mechanical properties including white matter stiffness.
- Traumatic Brain Injury** Intracranial injury caused by an external force that traumatically injures the brain; major cause of death and disability worldwide.
- White Matter** Inner core of the brain consists mainly of glial cells and myelinated axons; primarily associated with transmitting and modulating electrical signals between different brain regions; has a characteristic lighter color because of the high content of fatty white myelin; is believed to be anisotropic because of its highly organized axonal fibers tracts.

REFERENCES

- Abbot, N. J. (2004). Evidence for bulk flow of brain interstitial fluid: Significance for physiology and pathology. *Neurochemistry International*, *45*, 545–552.
- Alberts, B., Johnson, A., Lewis, J., Morgan, D., Raff, M., Roberts, K., & Walter, P. (2014). *Molecular biology of the cell* (6th ed.). New York, NY: Garland Science.
- Allen, H. G. (1969). *Analysis and design of structural sandwich panels*. Oxford: Pergamon Press.
- Ambrosi, D., Ateshian, G. A., Arruda, E. M., Cowin, S. C., Dumais, J., Goriely, A., & Garikipati, K. (2011). Perspectives on biological growth and remodeling. *Journal of the Mechanics and Physics of Solids*, *59*, 863–883.
- Bain, A. C., & Meaney, D. F. (2000). Tissue-level thresholds for axonal damage in an experimental model of central nervous system white matter injury. *Journal of Biomechanical Engineering*, *122*, 615–622.
- Bain, A. C., Raghupathi, R., & Meaney, D. F. (2001). Dynamic stretch correlates to both morphological abnormalities and electrophysiological impairment in a model of traumatic axonal injury. *Journal of Neurotrauma*, *18*, 499–511.
- Bardin, J. (2012). Neuroscience: Making connections. *Nature*, *483*, 394–396.
- Barkovich, A. J., Guerrini, R., Kuzniecky, R. I., Jackson, G. D., & Dobyns, W. B. (2012). A developmental and genetic classification for malformations of cortical development: Update 2012. *Brain*, *135*, 1348–1369.
- Bayly, P. V., Okamoto, R., Xu, G., Shi, Y., & Taber, L. A. (2013). A cortical folding model incorporating stress-dependent growth explains gyral wavelengths and stress patterns in the developing brain. *Physical Biology*, *10*, 016005.
- Bayly, P. V., Taber, L. A., & Kroenke, C. D. (2014). Mechanical forces in cerebral cortical folding: A review of measurements and models. *Journal of the Mechanical Behavior of Biomedical Materials*, *29*, 568–581.
- BenAmar, M., & Goriely, A. (2005). Growth and instability in elastic tissues. *Journal of the Mechanics and Physics of Solids*, *53*, 2284–2319.
- Bernal, R., Pullarkat, P. A., & Melo, F. (2007). Mechanical properties of axons. *Physical Review Letters*, *99*, 018301.
- Bilston, L. E. (2011). *Neural tissue biomechanics*. Heidelberg: Springer.

- Bilston, L. E., Liu, Z., & Phan-Thien, N. (2001). Large strain behavior of brain tissue in shear: Some experimental data and differential constitutive model. *Biorheology*, *38*, 335–345.
- Biot, M. A. (1957). Folding instability of a layered viscoelastic medium under compression. *Proceedings of the Royal Society of London A*, *242*, 444–454.
- Bray, D. (1984). Axonal growth in response to experimentally applied mechanical tension. *Developmental Biology*, *102*, 379–389.
- Budday, S., Kuhl, E., & Hutchinson, J. W. (2015). Period-doubling and period-tripling in growing bilayered systems. *Philosophical Magazine*, *95*, 3208–3224. <http://dx.doi.org/10.1080/14786435.2015.1014443>.
- Budday, S., Nay, R., de Rooij, R., Steinmann, P., Wyrobek, T., Ovaert, T. C., & Kuhl, E. (2014). Mechanical properties of gray and white matter brain tissue by indentation. *Journal of the Mechanical Behavior of Biomedical Materials*, *46*, 318–330.
- Budday, S., Raybaud, C., & Kuhl, E. (2014). A mechanical model predicts morphological abnormalities in the developing human brain. *Scientific Reports*, *4*, 5644.
- Budday, S., Steinmann, P., Goriely, A., & Kuhl, E. (2015). Size and curvature regulate pattern selection in the mammalian brain. *Extreme Mechanics Letters*, *4*, 193–198. <http://dx.doi.org/10.1016/j.eml.2015.07.004>.
- Budday, S., Steinmann, P., & Kuhl, E. (2014). The role of mechanics during brain development. *Journal of the Mechanics and Physics of Solids*, *72*, 75–92.
- Budday, S., Steinmann, P., & Kuhl, E. (2015a). Physical biology of human brain development. *Frontiers in Cellular Neuroscience*, *9*, 257. <http://dx.doi.org/10.3389/fncel.2015.00257>.
- Budday, S., Steinmann, P., & Kuhl, E. (2015b). Secondary instabilities modulate cortical complexity in the mammalian brain. *Philosophical Magazine*, *95*, 3244–3256. <http://dx.doi.org/10.1080/14786435.2015.1024184>.
- Buganza, A., & Kuhl, E. (2013). Review: Systems-based approaches towards wound healing. *Pediatric Research*, *73*, 553–563.
- Camarillo, D. B., Shull, P. B., Mattson, J., Shultz, R., & Garza, D. (2013). An instrumented mouthguard for measuring linear and angular head impact kinematics in American football. *Annals of Biomedical Engineering*, *41*, 1939–1949.
- Cater, H. L., Sundstrom, L. E., & Morrison, B., III (2006). Temporal development of hippocampal cell death is dependent on tissue strain but not strain rate. *Journal of Biomechanics*, *39*, 2810–2818.
- Chatelin, S., Constantinesco, A., & Willinger, R. (2010). Fifty years of brain tissue mechanical testing: From in vitro to in vivo investigations. *Biorheology*, *47*, 255–276.
- Christ, A. F., Franze, K., Gautier, H., Moshayedi, P., Fawcett, J., Franklin, R. J. M., & Guck, J. (2010). Mechanical differences between white and gray matter in the rat cerebellum measured by scanning force microscopy. *Journal of Biomechanics*, *43*, 2986–2992.
- Ciarletta, P., Balbi, V., & Kuhl, E. (2014). Pattern selection in growing tubular tissues. *Physical Review Letters*, *113*, 248101.
- Cloots, R. J. H., van Dommelen, J. A. W., Nyberg, T., Kleiven, S., & Geers, M. G. D. (2011). Micromechanics of diffuse axonal injury: Influence of axonal orientation and anisotropy. *Biomechanics and Modeling in Mechanobiology*, *10*, 413–422.
- Cloots, R. J. H., van Dommelen, J. A. W., Kleiven, S., & Geers, M. G. D. (2013). Multi-scale mechanics of traumatic brain injury: Predicting axonal strains from head loads. *Biomechanics and Modeling in Mechanobiology*, *12*, 137–150.
- De, S., Hwang, W., & Kuhl, E. (2015). *Multiscale modeling in biomechanics and mechanobiology*. London: Springer.
- Dennerll, T. J., Joshi, H. C., Steel, V. L., Buxbaum, R. E., & Heidemann, S. R. (1988). Tension and compression in the cytoskeleton of pc-12 neurites ii: Quantitative measurements. *Journal of Cellular Biochemistry*, *107*, 665–674.
- Dennerll, T. J., Lamoureux, P., Buxbaum, R. E., & Heidemann, S. R. (1989). The cytomechanics of axonal elongation and retraction. *Journal of Cellular Biochemistry*, *109*, 3073–3083.

- Dervaux, J., Ciarletta, P., & Ben Amar, M. (2009). Morphogenesis of thin hyperelastic plates: A constitutive theory of biological growth in the Föppl-von Kármán limit. *Journal of the Mechanics and Physics of Solids*, *57*, 458–471.
- Fallenstein, G. T., Hulce, V. D., & Melvin, J. W. (1969). Dynamic mechanical properties of human brain tissue. *Journal of Biomechanics*, *2*, 217–226.
- Feng, Y., Clayton, E. H., Chang, Y., Okamoto, R. J., & Bayly, P. V. (2013). Viscoelastic properties of the ferret brain measured in vivo at multiple frequencies by magnetic resonance elastography. *Journal of Biomechanics*, *46*, 863–870.
- Finlay, B. L., & Darlington, R. B. (1995). Linked regularities in the development and evolution of mammalian brains. *Science*, *268*, 1578–1584.
- Föppl, A. (1907). *Vorlesungenüber technische mechanik*, (Vol. 5). Leipzig: B.G. Teubner.
- Franceschini, G., Bigoni, D., Regitnig, P., & Holzapfel, G. A. (2006). Brain tissue deforms similarly to filled elastomers and follows consolidation theory. *Journal of the Mechanics and Physics of Solids*, *54*, 2592–2620.
- Franze, K. (2013). The mechanical control of nervous system development. *Development*, *140*, 3069–3077.
- Franze, K., Janmey, P. A., & Guck, J. (2013). Mechanics in neuronal development and repair. *Annual Review of Biomedical Engineering*, *15*, 227–251.
- Galford, J. E., & McElhaney, J. H. (1969). Some viscoelastic properties of scalp, brain and dura. *American Society of Mechanical Engineers, BHF*, *7*, 1–8.
- Garikipati, K., Arruda, E. M., Grosh, K., Narayanan, H., & Calve, S. (2004). A continuum treatment of growth in biological tissue: The coupling of mass transport and mechanics. *Journal of the Mechanics and Physics of Solids*, *52*, 1595–1625.
- Göktepe, S., Abilez, O. J., & Kuhl, E. (2010). A generic approach towards finite growth with examples of athlete's heart, cardiac dilation, and cardiac wall thickening. *Journal of the Mechanics and Physics of Solids*, *58*, 1661–1680.
- Goriely, A., Geers, M. G. D., Holzapfel, G. A., Jayamohan, J., Jerusalem, A., Sivaloganathan, S., & Kuhl, E. (2015). Mechanics of the brain: Perspectives, challenges, and opportunities. *Biomechanics and Modeling in Mechanobiology*, *14*, 931–965. <http://dx.doi.org/10.1007/s10237-015-0662-4>.
- Green, M. A., Bilston, L. E., & Sinkus, R. (2008). In vivo brain viscoelastic properties measured by magnetic resonance elastography. *NMR in Biomedicine*, *21*, 755–764.
- Hardan, A. Y., Jou, R. J., Keshavan, M. S., Varma, R., & Minshew, N. J. (2004). Increased frontal cortical folding in autism: A preliminary MRI study. *Psychiatry Research*, *131*, 263–268.
- Heidemann, S. R., Lamoureux, P., & Buxbaum, R. E. (1997). Cytomechanics of axonal development. *Cell Biochemistry and Biophysics*, *27*, 135–155.
- Herculano-Houzel, S. (2009). The human brain in numbers: A linearly scaled-up primate brain. *Frontiers in Human Neuroscience*, *3*, 31.1–31.11.
- Holland, M. A., Miller, K. E., & Kuhl, E. (2015). Emerging brain morphologies from axonal elongation. *Annals of Biomedical Engineering*, *43*, 1640–1653. <http://dx.doi.org/10.1007/s10439-015-1312-9>.
- Hrapko, M., van Dommelen, J. A. W., Peters, G. W. M., & Wismans, J. S. H. M. (2006). The mechanical behaviour of brain tissue: Large strain response and constitutive modelling. *Biorheology*, *43*, 623–636.
- Hrapko, M., van Dommelen, J. A. W., Peters, G. W. M., & Wismans, J. S. H. M. (2008). The influence of test conditions on characterisation of the mechanical properties of brain tissue. *Journal of Biomechanical Engineering*, *130*, 1–10.
- Ingber, D. E., Heidemann, S. R., Lamoureux, P., & Buxbaum, R. E. (2000). Opposing views on tensegrity as a structural framework for understanding cell mechanics. *Journal of Applied Physiology*, *89*, 1663–1678.

- Jérusalem, A., García-Grajales, J. A., Merchán-Perez, A., & Peña, J. M. (2014). A computational model coupling mechanics and electrophysiology in spinal cord injury. *Biomechanics and Modeling in Mechanobiology*, *13*, 883–896.
- Kachanov, L. M. (1958). On creep rupture time. *Izvestiya Akademii Nauk SSSR. Otdelenie Tekhnicheskikh Nauk*, *8*, 26–31.
- Kaster, T., Sack, I., & Samani, A. (2011). Measurement of the hyperelastic properties of ex vivo brain tissue slices. *Journal of Biomechanics*, *44*, 1158–1163.
- Kleiven, S. (2006). Evaluation of head injury criteria using a finite element model validated against experiments on localized brain motion, intracerebral acceleration, and intracranial pressure. *International Journal of Crashworthiness*, *11*, 65–79.
- Kleiven, S. (2007). Predictors for traumatic brain injury evaluated through accident reconstructions. *Stapp Car Crash Journal*, *51*, 1–35.
- Kleiven, S., & von Holst, H. (2002). Consequences of head size following trauma to the human head. *Journal of Biomechanics*, *35*, 153–160.
- Koser, D. E., Moeendarbary, E., Hanne, J., Kuerten, S., & Franze, K. (2015). CNS cell distribution and axon orientation determine local spinal cord mechanical properties. *Biophysical Journal*, *108*, 2137–2147.
- Kuhl, E., Menzel, A., & Steinmann, P. (2003). Computational modeling of growth—A critical review, a classification of concepts and two new consistent approaches. *Computational Mechanics*, *32*, 71–88.
- Kuhl, E., & Steinmann, P. (2003). Mass- and volume specific views on thermodynamics for open systems. *Proceedings of the Royal Society of London A*, *459*, 2547–2568.
- Lamoureux, P., Heidemann, S. R., & Miller, K. E. (2011). Mechanical manipulation of neurons to control axonal development. *Journal of Visualized Experiments*, *50*, 2509.
- Lamoureux, P., Heidemann, S. R., Martzke, N. R., & Miller, K. E. (2010). Growth and elongation within and along the axon. *Developmental Neurobiology*, *70*, 135–149.
- Lang, G., Stewart, P. S., Vella, D., Waters, S. L., & Goriely, A. (2014). Is the donnan effect sufficient to explain swelling in brain tissue slices? *Journal of the Royal Society Interface*, *11*, 20140123.
- Le Gros Clark, W. E. (1945). Deformation patterns in the cerebral cortex. In W. E. Le Gros Clark & P. B. Medawar (Eds.), *Essays on growth and form* (pp. 1–22). London: Oxford University Press.
- Lemaître, J. (1992). *A course on damage mechanics*. Berlin: Springer.
- Lemaître, J., & Chaboche, J. L. (1985). *Mécanique des matériaux solides*. Paris: Dunod.
- Li, B., Cao, Y. P., Feng, X. Q., & Gao, H. (2012). Mechanics of morphological instabilities and surface wrinkling in soft materials: A review. *Soft Matter*, *8*, 5728–5745.
- Macyszyn, L., Akbari, H., Pisapia, J. M., Da, X., Attiah, M., Pigrish, V., & Davatzikos, C. (2015). Imaging patterns predict patient survival and molecular subtype in glioblastoma via machine learning techniques. *Neuro-Oncology*. <http://dx.doi.org/10.1093/neuonc/nov127>.
- McIntosh, T. K., Saatman, K. E., Raghupathi, R., Graham, D. I., Smith, D. H., Lee, V. M. Y., & Trojanowski, J. Q. (1998). The molecular and cellular sequelae of experimental traumatic brain injury: Pathogenetic mechanisms. *Neuropathology and Applied Neurobiology*, *24*, 251–267.
- Meaney, D. F., Morrison, B., & Bass, C. D. (2014). The mechanics of traumatic brain injury: A review of what we know and what we need to know for reducing its social burden. *Journal of Biomechanical Engineering*, *136*, 021008.1–021008.14.
- Memarian, N., Kim, S., Dewar, S., Engel, J., & Staba, R. J. (2015). Multimodal data and machine learning for surgery outcome prediction in complicated cases of mesial temporal lobe epilepsy. *Computers in Biology and Medicine*, *64*, 67–78.
- Mihai, L. A., Chin, L. K., Janmey, P. A., & Goriely, A. (2015). A hyperelastic constitutive model for compression stiffening applicable to brain and fat tissues. *Journal of the Royal Society Interface*, *12*, 20150486.

- Miller, K. (2011). *Biomechanics of the brain*. New York, NY: Springer.
- Miller, K., & Chinzei, K. (1997). Constitutive modelling of brain tissue: Experiment and theory. *Journal of Biomechanics*, *30*, 1115–1121.
- Miller, K., & Chinzei, K. (2002). Mechanical properties of brain tissue in tension. *Journal of Biomechanics*, *35*, 483–490.
- Mooney, M. (1940). A theory of large elastic deformation. *Journal of Applied Physics*, *11*, 582–592.
- Morrison, B., III, Saatman, K., Meaney, D., & McIntosh, T. (1998). In vitro central nervous system models of mechanically induced trauma: A review. *Journal of Neurotrauma*, *15*, 911–928.
- Mullins, L. (1969). Softening of rubber by deformation. *Rubber Chemistry and Technology*, *42*, 339–362.
- National Highway Traffic Safety Administration (1972). *Occupant crash protection—head injury criterion*. Washington, DC: NHTSA. (S6.2 of FMVSS 571.208).
- Nolte, J. (2009). *The human brain: An introduction to its functional anatomy* (6th ed.). Philadelphia, PA: Mosby Elsevier.
- Ogden, R. W. (1972). Large deformation isotropic elasticity—On the correlation of theory and experiment for incompressible rubberlike solids. *Proceedings of the Royal Society of London A*, *326*, 565–584.
- Ogden, R. W. (1984). *Non-linear elastic deformations*. Chichester: Ellis Horwood.
- Ogden, R. W., & Roxburgh, D. G. (1999). A pseudo-elastic model for the mullins effect in filled rubber. *Proceedings of the Royal Society of London A*, *455*, 2861–2877.
- Oliver, W. C., & Pharr, G. M. (2004). Measurement of hardness and elastic modulus by instrumented indentation: Advances in understanding and refinements to methodology. *Journal of Materials Research*, *19*, 3–20.
- O'Toole, M., Lamoureux, P., & Miller, K. E. (2008). A physical model of axonal elongation: Force, viscosity, and adhesions govern the mode of outgrowth. *Biophysical Journal*, *94*, 2610–2620.
- Pervin, F., & Chen, W. W. (2009). Dynamic mechanical response of bovine gray matter and white matter brain tissues under compression. *Journal of Biomechanics*, *42*, 731–735.
- Pfister, B. J., Iwata, A., Meaney, D. F., & Smith, D. H. (2004). Extreme stretch growth of integrated axons. *The Journal of Neuroscience*, *24*, 7978–7983.
- Pogoda, K., Chin, L. K., Georges, P. C., Byfield, F. J., Bucki, R., Kim, R., & Janney, P. A. (2014). Compression stiffening of brain and its effect on mechanosensing by glioma cells. *New Journal of Physics*, *16*, 075002.
- Prange, M. T., & Margulies, S. S. (2002). Regional, directional, and age-dependent properties of the brain undergoing large deformation. *Journal of Biomechanical Engineering*, *124*, 244–252.
- Prevost, T. P., Balakrishnan, A., Suresh, S., & Socrate, S. (2011). Biomechanics of brain tissue. *Acta Biomater*, *7*, 83–95.
- Prins, M. L., Alexander, D., Giza, C. C., & Hovda, D. A. (2013). Repeated mild traumatic brain injury: Mechanisms of cerebral vulnerability. *Journal of Neurotrauma*, *30*, 30–38.
- Rashid, B., Destrade, M., & Gilchrist, M. D. (2013). Mechanical characterization of brain tissue in simple shear at dynamic strain rates. *Journal of the Mechanical Behavior of Biomedical Materials*, *28*, 71–85.
- Raybaud, C., Ahmad, T., Rastegar, N., Shroff, M., & Al Nassar, M. (2013). The premature brain: Developmental and lesional anatomy. *Neuroradiology*, *55*, S23–S40.
- Raybaud, C., & Widjaja, E. (2011). Development and dysgenesis of the cerebral cortex: Malformations of cortical development. *Neuroimaging Clinics of North America*, *21*, 483–543.
- Richman, D. P., Stewart, R. M., Hutchinson, J. W., & Caviness, V. S. (1975). Mechanical model of brain convolitional development. *Science*, *189*, 18–21.

- Rivlin, R. S. (1948). Large elastic deformations of isotropic materials. IV. Further developments of the general theory. *Philosophical Transactions of the Royal Society of London A*, 241, 379–397.
- Rodriguez, E. K., Hoger, A., & McCulloch, A. D. (1994). Stress-dependent finite growth in soft elastic tissues. *Journal of Biomechanics*, 27, 455–467.
- Roossien, D. H., Lamoureux, P., & Miller, K. E. (2014). Cytoplasmic dynein pushes the cytoskeletal meshwork forward during axonal elongation. *Journal of Cell Science*, 127, 3593–3602.
- Sack, I., Beierback, B., Wuerfel, J., Klatt, D., Hamhaber, U., Papazoglou, S., & Braun, J. (2009). The impact of aging and gender on brain viscoelasticity. *NeuroImage*, 46, 652–657.
- Simo, J. C., & Ju, J. W. (1987). Strain- and stress based continuum damage models: Part I—Formulation, Part II—Computational aspects. *International Journal of Solids and Structures*, 23, 821–869.
- Smart, I., & McSherry, G. (1986). Gyrus formation in the cerebral cortex in the ferret. I. Description of the external changes. *Journal of Anatomy*, 146, 141–152.
- Songbai, J., Ghadyani, H., Bolander, R., Beckwith, J. G., Ford, J. C., McAllister, T. W., & Greenwald, R. M. (2014). Parametric comparisons of inter cranial mechanical responses from three validated finite element models for the human head. *Annals of Biomedical Engineering*, 42, 11–24.
- Streitberger, K. J., Sack, I., Krefling, D., Pfuller, C., Braun, J., Friedemann, P., & Wurfel, J. (2012). Brain viscoelasticity alteration in chronic-progressive multiple sclerosis. *PLoS ONE*, 7, e29888.
- Sun, T., & Hevner, R. F. (2014). Growth and folding of the mammalian cerebral cortex: From molecules to malformations. *Nature Reviews Neuroscience*, 15, 217–232.
- Suo, Z. (2012). Mechanics of stretchable electronics and soft machines. *MRS Bulletin*, 37, 218–225.
- Suter, D. M., & Miller, K. E. (2011). The emerging role of forces in axonal elongation. *Progress in Neurobiology*, 94, 91–101.
- Takhounts, E. G., Eppinger, R. H., Campbell, J. Q., & Tannous, R. E. (2003). On the development of the SIMon finite element head model. *Stapp Car Crash Journal*, 47, 107–133.
- Tang-Schomer, M. D., Patel, A. R., Baas, P. W., & Smith, D. H. (2010). Mechanical breaking of microtubules in axons during dynamic stretch injury underlies delayed elasticity, microtubule disassembly, and axon degeneration. *FASEB Journal*, 24, 1401–1410.
- van Bork-Feltkamp, A. J. (1930). *Uitkomsten van een onderzoek van een 60-tal hersenen van chineezen*. Amsterdam: Versluy.
- van Dommelen, J. A. W., van der Sande, T. P. J., Hrapko, M., & Peters, G. W. M. (2010). Mechanical properties of brain tissue by indentation: Interregional variation. *Journal of the Mechanical Behavior of Biomedical Materials*, 3, 158–166.
- van den Bedem, H., & Kuhl, E. (2015). Tau-ism: the Yin and Yang of the microtubule sliding, detachment, and rupture. *Biophysical Journal*. <http://dx.doi.org/10.1016/j.bpj.2015.10.020>.
- Van Essen, D. C. (1997). A tension-based theory of morphogenesis and compact wiring in the central nervous system. *Nature*, 385, 313–318.
- von Kármán, T. (2010). Festigkeitsproblem im Maschinenbau. *Encyklopadie der Mathematischen Wissenschaftler*, 4, 311–385.
- Welker, W. (1990). Why does cerebral cortex fissure and fold? A review of determinants of gyri and sulci. In E. G. Jones & A. Peters (Eds.), *Cerebral cortex: Vol. 8B*. (pp. 3–136). New York, NY: Springer Science+Business Media.
- Welker, W., Johnson, I. J., & Noe, A. (2014). *Comparative mammalian brain collections*. Retrieved from, <http://brainmuseum.org>.

- Wisco, J. J., Kuperberg, G., Manoach, D., Quinn, B. T., Busa, E., Fischl, B., & Sorensen, A. G. (2007). Abnormal cortical folding patterns within broca's area in schizophrenia: Evidence from structural MRI. *Schizophrenia Research*, *94*, 317–327.
- Xu, G., Knutsen, A. K., Dikranian, K., Kroenke, C. D., Bayly, P. V., & Taber, L. A. (2010). Axons pull on the brain, but tension does not drive cortical folding. *Journal of Biomechanical Engineering*, *132*, 071013.
- Zöllner, A. M., Abilez, O. J., Böhl, M., & Kuhl, E. (2012). Stretching skeletal muscle: Chronic muscle lengthening through sarcomerogenesis. *PLoS ONE*, *7*, e45661.
- Zöllner, A. M., Holland, M. A., Honda, K. S., Gosain, A. K., & Kuhl, E. (2013). Growth on demand: Reviewing the mechanobiology of stretched skin. *Journal of the Mechanical Behavior of Biomedical Materials*, *28*, 495–509.

